

Measurement of the Ratio G_E^n/G_M^n by the Double-polarized $^2\text{H}(\vec{e}, e'\vec{n})$ Reaction

An experimental proposal to Jefferson Lab. PAC 45.

May 21, 2017

J.R.M. Annand¹, D.J. Hamilton, K. Hamilton, D.G. Ireland,
I.J.D. MacGregor, R. Montgomery, B. Seitz, D. Sokhan
University of Glasgow, Glasgow G12 8QQ, UK.

B. Wojtsekhowski, B Sawatzky, A. Camsonne, J.P. Chen, J. Gomez,
O. Hansen, D. Higinbotham, M. Jones, C. Keppel, R. Michaels, K. Park
*Thomas Jefferson National Accelerator Facility, Newport News, VA 23606,
USA.*

N. Piskunov, D. Kirillov, A. Kovalenko, K. Legostaeva, A. Livanov, J.
Mushinsky, I. Sitnik, R. Shindin
Joint Institute for Nuclear Research, Dubna, Russian Federation.

V. Bellini, P. Castorina, V. Kuznetsov, F. Mammoliti, L. Re, G. Russo, M.
Russo, A. Shahinyan, C.M. Sutera, F. Tortorici
INFN Catania, Italy.

M. Kohl, K. Al Amin, D. Biswas, T. Cao, E. Christy, B. Dongwi, T. Gautam,
P. Gueye, A. Liyanage, L. Harris, N. Lashley-Colthirst, A. Nadeeshani, J.
Nazeer, B. Pandey, L. Tang
Hampton University, Hampton, VA 23668, USA

E. Brash, P. Monaghan
Christopher Newport University, Newport News, VA 23606, USA

G. Cates, K. Gnanvo, N. Liyanage, V. Nelyubin, H. Nguyen
University of Virginia, Charlottesville, VA 22901, USA

J. C. Cornejo, G. B. Franklin, B. Quinn
Carnegie Mellon University, Pittsburgh, PA 15213, USA

E. Cisbani, F. De Persio, F. Garibaldi, F. Meddi, G.M. Urciuoli
INFN Rome, Italy

¹Corresponding author: john.annand@glasgow.ac.uk

31 T. Averett, C. Ayerbe Gayoso, C. Perdrisat
 32 *College of William and Mary, Williamsburg, VA, USA*

33 A. Asaturyan, A. Mkrtchyan, H. Mkrtchyan, V. Tadevosyan, A. Shahinyan, H.
 34 Voskanyan, S. Zhamkochyan
 35 *A.I. Alikhanyan National Science Laboratory, Yerevan 0036, Armenia*

36 A. J. R. Puckett, E. Fuchey, F. Obrecht
 37 *University of Connecticut, Storrs, CT 06269, USA*

38 S. Riordan
 39 *Argonne National Laboratory, Argonne, IL 60439, USA*

40 A. Ahmidouch, S. Danagouliau
 41 *North Carolina A&T State University, Greensboro, NC 27411, USA*

42 G. Niculescu, I. Niculescu
 43 *James Madison University, Harrisonburg, VA 22807, USA*

44 V. Punjabi
 45 *Norfolk State University, Norfolk, VA 23504, USA*

46 W. Tireman
 47 *Northern Michigan University, Marquette, Michigan 49855, USA*

48 D. Androic
 49 *University of Zagreb, Zagreb, HR-10000, Croatia*

50 E. Long
 51 *University of New Hampshire, Durham, NH 03824, USA*

52 N. Kalantarians
 53 *Virginia Union University, Richmond VA, 23220, USA*

54 P. King
 55 *Ohio University, Athens, OH 45701, USA*

56 G. De Cataldo, R. De Leo, D. Di Bari, L. Lagamba, E. Nappi
 57 *INFN Bari, Italy*

58 I. Balossino, L. Barion, G. Ciullo, M. Contalbrigo, A. Drago, P. Lenisa, A.
 59 Movsisyan, L.L. Pappalardo, F. Spizzo, M. Turisini
 60 *INFN Ferrara, Italy*

61 E. De Sanctis, D. Hasch, V. Lucherini, M. Mirazita, P. Rossi
 62 *INFN LNF, Italy*

63 M. Carpinelli, A. Gabrieli, G. Maccioni, M. Sant, V. Sipala
 64 *INFN LNS, Italy*

65 M. Battaglieri, G. Bracco, A. Celentano, R. De Vita, E. Fanchini, L.
66 Marsicano, P. Musico, M. Osipenko, M. Ripani, M. Taiuti
67 *INFN Genova, Italy*

68 R. Perrino
69 *INFN Lecce, Italy*

70 G. Simi
71 *INFN Padova, Italy*

72 A. Del Dotto
73 *INFN Rome, Italy & University of South Carolina, USA*

74 A. D'Angelo, L. Lanza, A. Rizzo
75 *INFN Rome Tor Vergata, Italy*

76 A. Filippi, M. Genovese
77 *INFN Torino, Italy*

78 *and*
79 **The Hall-A Collaboration** of
80 *Thomas Jefferson National Accelerator Facility.*

Abstract

We propose a measurement of double polarized $^2\text{H}(\vec{e}, e'\vec{n})$ at a four-momentum transfer $Q^2 = 4.5 \text{ (GeV/c)}^2$. The ratio of electric to magnetic elastic form factors G_E^n/G_M^n will be extracted from the ratio of transverse and longitudinal components of the spin polarization P_x/P_z , which is transferred to the recoiling neutron from an incident, longitudinally polarized electron.

The experiment will be performed in Hall-A of Jefferson Laboratory, utilizing common components of the Super BigBite apparatus. It will include apparatus to implement neutron polarimetry, using both $np \rightarrow pn$ (charge-exchange) and $np \rightarrow np$ scattering to analyze the neutron polarization. The electron arm will be the BigBite spectrometer. The hadron arm will be the neutron polarimeter consisting of a Cu block (the analyzer), GEM charged particle trackers, the CDet coordinate detector, the hadron calorimeter HCAL and a set of scintillation counters. The bulk of this apparatus is currently under commissioning for other approved SBS experiments. The polarimeter will be sensitive both to high-momentum forward-angle protons, to enable it to measure charge-exchange $np \rightarrow pn$ scattering, and to large-angle, low-momentum protons, to enable it to measure $np \rightarrow np$ scattering. A recent measurement at JINR Dubna has shown that $np \rightarrow pn$ on a relatively heavy nucleus has a sizable analyzing power, similar to $np \rightarrow pn$ scattering on the proton. The proposed polarimeter will yield valuable information on the figure of merit for both $np \rightarrow pn$ and $np \rightarrow np$ scattering channels.

The present experiment, which we propose to run concurrently with E12-09-019, will yield G_E^n/G_M^n at the highest Q^2 kinematic point yet recorded. The technical information on the polarimetry will be used to optimize future measurements of G_E^n/G_M^n in Hall A and/or Hall C to reach Q^2 values as high as 9.3 (GeV/c)^2 using recoil polarimetry techniques.

Contents

118	1 Introduction	8
119	1.1 Physics Motivation	8
120	1.2 The scaling behavior of EMFF and non-perturbative QCD	9
121	1.2.1 Dyson Swinger Equation Framework	10
122	1.2.2 Nambu-Jona-Lasinio Model	12
123	1.2.3 Light Front Holographic QCD	12
124	1.2.4 The link with Generalized Parton Distributions	12
125	1.3 Previous EMFF Measurements	13
126	1.3.1 Unpolarized	13
127	1.3.2 Polarized Target	13
128	1.3.3 Recoil Polarimetry	14
129	1.4 Related EMFF Measurements at JLab.	14
130	1.4.1 E12-11-009: <i>The Neutron Electric Form Factor at</i>	
131	<i>Q^2 up to $7(\text{GeV}/c)^2$ from the Reaction $^2\text{H}(\vec{e}, e' \vec{n})$</i>	
132	<i>via Recoil Polarimetry</i>	14
133	1.4.2 E12-09-016: <i>Measurement of the Neutron Electro-</i>	
134	<i>magnetic Form Factor Ratio G_E^n/G_M^n at high Q^2 . .</i>	15
135	1.4.3 E12-09-019: <i>Precision Measurement of the Neutron</i>	
136	<i>Magnetic Form Factor up to $Q^2 = 13.5 (\text{GeV}/c)^2$. .</i>	15
137	1.4.4 E12-07-109: <i>Large Acceptance Proton Form Factor</i>	
138	<i>Ratio Measurements at High Q^2 using the Recoil Po-</i>	
139	<i>larization Method [3].</i>	16
140	1.4.5 E12-07-108: <i>Precision measurement of the Proton</i>	
141	<i>Elastic Cross Section at High Q^2</i>	16
142	1.4.6 E12-07-104: <i>Measurement of the Neutron Magnetic</i>	
143	<i>Form Factor at High Q^2 Using the Ratio Method on</i>	
144	<i>Deuterium</i>	16
145	2 Double-Polarized Measurements of G_E/G_M	16
146	2.1 Polarized Beam and Recoil Polarimetry	17
147	2.2 Nucleon Polarimetry	18
148	2.2.1 Neutron analyzing power at several GeV/c	19
149	2.2.2 Experimental data for polarized nucleon-nucleon scat-	
150	tering	19
151	2.2.3 The Figure of Merit for neutron polarimetry	20
152	3 Experimental Method	22
153	3.1 The e' Spectrometer BigBite	24
154	3.1.1 Dipole Magnet	24
155	3.1.2 Front and Rear GEM Trackers	25
156	3.1.3 GRINCH Gas Cherenkov	25
157	3.1.4 Timing Hodoscope	26
158	3.1.5 Pb-Glass Calorimeter	26
159	3.2 The Neutron Polarimeter	26
160	3.2.1 The Cu Analyzer	27
161	3.2.2 The GEM Charged Particle Tracker	27
162	3.2.3 The HCAL Hadron Calorimeter	28
163	3.2.4 Rear Detector for Charged-Particle Identification	29
164	3.2.5 Large-Angle Proton Detection	29
165	3.2.6 The 48D48 Dipole	30

166	4 Monte Carlo Simulations of the Polarimeter	31
167	4.1 Neutron Spin Precession	31
168	4.2 Separation of neutrons from protons	32
169	4.3 Polarimeter Angle Reconstruction	33
170	4.4 Determination of G_E^n/G_M^n from Simulated Azimuthal Asym-	
171	metries	35
172	4.5 Kinematics	37
173	4.6 Background Rates and the Trigger Rate	38
174	4.7 Inelastic Background Rejection	41
175	4.8 Systematic Uncertainties	42
176	5 Estimates of Experimental Precision	43
177	6 Beam Time Request	44
178	6.0.1 $Q^2 = 4.5 \text{ (GeV/c)}^2$	45
179	6.0.2 $Q^2 = 6.0, 9.3 \text{ (GeV/c)}^2$	45
180	7 Summary and Comparison with other G_E^n/G_M^n measure-	
181	ments at Jefferson Lab.	46

Foreword

This proposal builds on the work of LOI12-15-003 and an earlier deferred proposal PR12-12-012. The response of PAC 43 to LOI12-15-003 appears in the final PAC report as follows:

Issues: The TAC raised a number of issues including high rate for the DAQ and backgrounds in the neutron arm. The proposed method in general is the same as what is proposed in the already approved E12-11-009, and the proposed improvement in the FOM of the recoil neutron polarimeter if demonstrated will benefit E12-11-009. There is also an approved Experiment E12-09-016 using a polarized ^3He target which allows for an extraction of the neutron electric form factor in excess of $Q^2=10 \text{ (GeV/c)}^2$. While the PAC believes in the importance of extending the G_E^n determination from the deuteron to a Q^2 value comparable to that of E12-09-016, the PAC does not believe there should be parallel efforts in pursuing the same experimental technique.

Recommendation: The proponents are encouraged to work with the lab management and the E12-11-009 collaboration to improve the FOM of the recoil neutron polarimeter in order to optimize the measurements using the already approved beam time of E12-11-009.

The SBS and C-GEN (E12-11-009) proponents of G_E^n/G_M^n by recoil-neutron polarimetry have been discussing neutron polarimetry techniques since the PAC's response to LOI12-15-003 was received. This experiment is aimed at addressing some of the questions (analyzing power, rates, etc....) associated with the $np \rightarrow pn$ charge-exchange approach within the SBS apparatus. Experience and data from this staged approach will be used to develop the optimal combination of techniques to measure G_E^n at the largest Q^2 in either Hall A or Hall C.

In addition, this measurement will, in a relatively short beam time, provide G_E^n/G_M^n at the highest value of Q^2 yet attained worldwide.. We propose an initial run at a single $Q^2 = 4.5 \text{ (GeV/c)}^2$ point. This would run concurrently with the G_M^n/G_M^p experiment, and the kinematic point would be one in the E12-09-019 sequence. The experiment would be adapted to G_E^n/G_M^n by insertion of polarimeter components on the hadron arm.

While the present proposal requests beam time for one data point only, a study of two additional points at $Q^2 = 6.0, 9.3 \text{ (GeV/c)}^2$ is included to demonstrate the potential to reach high values of Q^2 . This study is based on new measurements of polarized, charge-exchange neutron scattering from nuclei at JINR Dubna. Preliminary results from this experiment confirm that, similar to the free $np \rightarrow pn$ case, charge-exchange scattering from nuclei has a high analyzing power at neutron momenta of several GeV/c. This offers a path to high-precision measurements at high Q^2 . There is no comparable data on polarized "standard" $np \rightarrow np$ scattering and it will be immensely valuable to have this information to determine the optimum setup for future, high- Q^2 operation.

1 Introduction

The understanding of nucleon structure and the nature of quark confinement is one of the central goals facing nuclear physics today. At the $\sim fm$ scales typical of hadrons, quantum chromodynamics (QCD), the field theory describing the quark-gluon interaction, is too strong to be solved by perturbative methods (pQCD) and the understanding of non-perturbative QCD remains a pivotal problem of theoretical physics.

One of the critical factors driving progress in understanding nucleon structure is the availability of high precision electron scattering results over a broad range of Q^2 . The higher Q^2 domain is relatively unexplored, especially for the neutron, and thus has immense potential to discriminate between different nucleon structure models. Elastic form factors remain a major source of information about quark distributions at small transverse distance scales and the Q^2 dependence of G_E^p/G_M^p has generated more theoretical papers than any other result to come out of Jefferson Laboratory (JLab). There is considerable anticipation regarding new results that push both G_E^p/G_M^p and G_E^n/G_M^n to higher values of Q^2 .

The Super-Bigbite-Spectrometer (SBS) experimental program has three approved measurements of nucleon elastic form factors [1, 2, 3]. In addition E12-07-108 [4] has measured G_M^p up to high Q^2 , using the Hall-A HRS spectrometers to achieve a 2-4% measurement of the $e - p$ elastic scattering cross section. In Hall C, a measurement [5] of G_E^n/G_M^n using the SHMS and a custom neutron polarimeter has been approved. Thus extraction of absolute values of G_M^n , G_E^p and G_E^n from ratio measurements will be possible. A major strength of the JLab program is the ability to measure all four of the Electromagnetic Form Factors (EMFF), with sufficient accuracy and reach in Q^2 to address some of the most fundamental and topical questions in hadronic physics.

We propose a high-precision measurement of G_E^n/G_M^n at $Q^2 = 4.5 \text{ (GeV/c)}^2$, by quasi-elastic ${}^2\text{H}(\vec{e}, e'\vec{n})$, with the intention of evaluating the best combination of reaction channels and detector systems for measurements at higher Q^2 . If a recoil polarimetry experiment can eventually reach $Q^2 = 9.3 \text{ (GeV/c)}^2$ this will almost triple the Q^2 range currently covered by published data [6] and overlap well with the new experiment E12-09-016 [1]. Ref. [6, 1] both employ ${}^3\text{He}(\vec{e}, n)$, while existing ${}^2\text{H}(\vec{e}, e'\vec{n})$ data [7] extend up to $Q^2 = 1.5 \text{ (GeV/c)}^2$ only. Neutron measurements are technically very challenging and must employ quasi-free scattering from light nuclei, which introduces some uncertainty in extrapolation to the free-neutron case. However identification of the quasi elastic channel is more straightforward for ${}^2\text{H}$ compared to ${}^3\text{He}$. By employing different experimental techniques, with different systematic effects, and different light-nucleus (“neutron”) targets, with different binding and final state interaction effects, one obtains an extremely valuable cross check on the accuracy of the measurements.

1.1 Physics Motivation

In the one-photon exchange approximation the most general form of a relativistically covariant hadronic current for a spin-1/2 nucleon, which satisfies current conservation, is:

$$J_{hadronic}^\mu = e\bar{N}(p') \left[\gamma^\mu F_1(Q^2) + \frac{i\sigma^{\mu\nu}q_\nu}{2M} F_2(Q^2) \right] \quad (1)$$

where $\bar{N}(p')$ is the nucleon Dirac spinor for the final momentum p' , and $F_1(Q^2)$ and $F_2(Q^2)$ are the Dirac (helicity conserving) and Pauli (helicity flip) form factors. It is often convenient to express cross sections and other observables in terms of the Sachs electric (G_E) and magnetic (G_M) form factors which are linear combinations of F_1 and F_2 .

$$G_E = F_1 - \tau F_2 \quad G_M = F_1 + F_2 \quad (2)$$

where $\tau = Q^2/4M_N^2$. G_E and G_M represent, in the Breit frame, the Fourier transforms of the distributions of charge and magnetic moment respectively of the nucleon constituents.

The EMFF (F_1 , F_2 or alternatively G_E , G_M) are among the simplest of hadron-structure observables, but none the less they continue to play a vital role in constraining non-perturbative QDC treatments of nucleon structure. Lattice QDC techniques continue to make big strides towards an accurate representation of the EMFF. However calculations of this type are still limited to relatively low values of Q^2 for the nucleon, although for the pion they now overlap well with the kinematic domain accessible at JLab. The EMFF also provide an indispensable constraint to Generalized Parton Distribution (GPD) analyses to extract the “3D” structure of the nucleon as outlined in Sec.1.2.4.

1.2 The scaling behavior of EMFF and non-perturbative QCD

On the basis of quark counting rules F_1 is expected to scale as $1/Q^4$, while F_2 is supposed to scale as $1/Q^6$ [8] at sufficiently high values of Q^2 . After publication of Ref.[9], it became clear that F_2^p/F_1^p did not scale as $1/Q^2$, as evident in Fig.1 (Left). The difference in apparent scaling behavior of proton data derived from double-polarized measurements [9, 10, 11, 12, 13], as opposed to Rosenbluth separation of differential cross sections [14, 15, 16], has been attributed to two-photon exchange effects. If these constitute a significant effect, Rosenbluth separation will be highly sensitive, while double-polarized measurements should be relatively insensitive.

The behaviour of the neutron G_E^n/G_M^n ratio (Fig. 2) is quite different from the proton and unknown for $Q^2 > 3.4$ (GeV/c)². Measurements of all four Sachs form factors, provide the means to make a flavor separation to obtain the Dirac and Pauli form factors of the u and d quarks: $F_{1,2}^u$, $F_{1,2}^d$ respectively. Assuming negligible nucleon strange content they are linear combinations of the proton and neutron form factors:

$$F_{1,2}^u(Q^2) = F_{1,2}^n + 2F_{1,2}^p \quad F_{1,2}^d(Q^2) = 2F_{1,2}^n + F_{1,2}^p \quad (3)$$

The kinematic range over which such a separation is possible is limited by the range of G_E^n , which emphasizes the importance of measuring neutron as well as proton distributions with high precision. The first flavor separation [17] to

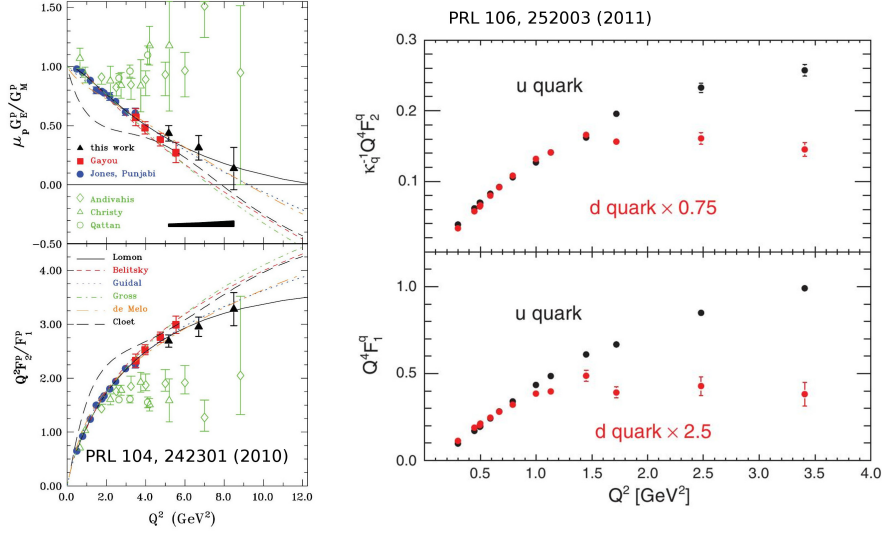


Figure 1: *Left* Q^2 scaling of the proton form factors from Ref[12] compared to theoretical predictions. The blue, red, black data points [9, 10, 12] are JLab double polarized data. The open green data points from SLAC [14] and JLab [15, 16] were obtained by unpolarized Rosenbluth separation. *Right* Q^2 scaling of the separated u, d form factors from Ref. [17].

incorporate Hall-A G_E^n/G_M^n data [6] up to 3.4 (GeV/c)² shows an intriguing difference in scaling behavior between the u and d quarks (Fig. 1 Right). Above ~ 1 (GeV/c)², $F_{1,2}^d$ appears to scale roughly as $1/Q^4$, whereas $F_{1,2}^u$ appears to scale roughly as $1/Q^2$.

Ultimately lattice QCD is expected to provide the best theoretical description of the Q^2 evolution of the EMFF, and indeed new calculations on the pion [18] reach up to $Q^2 = 6$ (GeV/c)², coinciding with JLab experiment E12-06-101. However accurate baryon calculations are not possible at medium to high Q^2 as the numerical overheads become too great. Alternatively QCD-compatible calculations of baryon structure may use effective degrees of freedom such as constituent quarks.

1.2.1 Dyson Swinger Equation Framework

One theoretical technique has come to prominence in the past decade. It is based on the infinite series of Dyson-Schwinger Equations (DSE) that interrelate the Green's functions of QCD [19]. Recent calculations explicitly describe the dynamical generation of the mass of constituent quarks, and show excellent agreement with available lattice QCD results. Using the dressed quarks as the elementary degrees of freedom, the nucleon form factors may be calculated using a Poincaré covariant Faddeev equation (DSE/F) [20]. While still an approximation, the DSE/F approach is based on first principles. It is limited, however, in that precisely three constituent quarks are considered, so that for instance pion-cloud effects are not investigated. However, it is reasonable to assume the

dominance of the 3-quark component of the wave function at relatively high values of Q^2 .

Building on the work of Ref.[20] a unified study of nucleon and Δ elastic and transition form factors has recently been made [21], which provides (Fig. 2) a consistent description of both $\mu_p G_E^p/G_M^p$ and $\mu_n G_E^n/G_M^n$ and predicts for both a zero-crossing point. The location of the zero crossing point (if it exists) of the ratios has implications for the location and width of the transition region between constituent- and parton-like behavior of the dressed quarks. A more rapid transition from non-perturbative to perturbative behavior pushes the proton zero point to higher Q^2 , while conversely the neutron zero point is pushed to lower Q^2 . Thus the ability of the JLab EMFF measurements to push into the $Q^2 \sim 10 (GeV/c)^2$ domain will have a major impact in testing theoretical predictions of this type. In the case of the neutron the kinematic region of interest is completely unexplored.

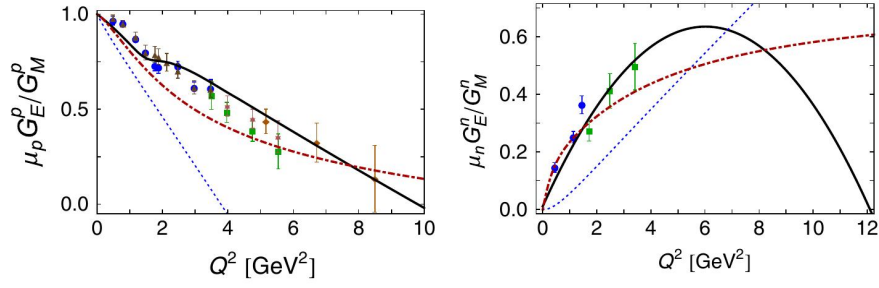


Figure 2: Left: “QCD-kindred” calculation [21] (black line) of $\mu_p G_E^p/G_M^p$ compared to JLab data [9, 10, 11, 12, 13]. Right: equivalent calculation of $\mu_n G_E^n/G_M^n$ (black line) compared to JLab. data [6, 7]. Red dot-dash lines are from Ref. [57], and blue dotted lines from Ref. [22].

Within the framework of Ref.[21] di-quark correlations are behind the zero-crossing behavior of G_E/G_M .

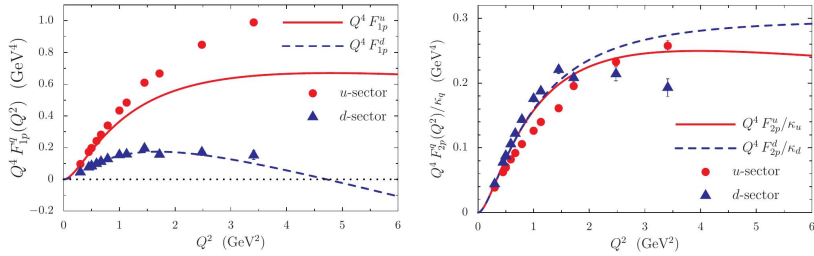


Figure 3: Left: Scaling behavior of F_1 and F_2 for u and d quarks. Data from Ref. [17], curves from the NJL calculation of Ref. [23]

344 1.2.2 Nambu-Jona-Lasinio Model

345 Flavor-separated scaling behavior is addressed in Ref. [21] and also in a cal-
 346 culation made within the framework of a covariant, confining Nambu-Jona-
 347 Lasinio (NJL) model [23]. For F_1 the dominance of the u-quark sector is in-
 348 terpreted as a consequence of scalar di-quark correlations, which play a smaller
 349 role in the d-quark sector. The u-d difference for F_2 is less dramatic, due to
 350 axial-vector diquark and pion-cloud contributions to the d sector, counteract-
 351 ing the effect of the scalar di-quark correlation. The comparison with data is
 352 limited to $Q^2 \leq 3.4 \text{ (GeV/c)}^2$, above which there is no data on G_E^n . Precise
 353 new neutron data at $Q^2 > 3.4 \text{ (GeV/c)}^2$ and confirmation of the behavior at
 354 $1.5 < Q^2 < 3.5 \text{ (GeV/c)}^2$ are required to test further these new theoretical
 355 developments.

356 1.2.3 Light Front Holographic QCD

357 Recently an analysis of the nucleon EMFF has been made within the framework
 358 of light-front holographic QCD [24]. The helicity-conserving and helicity-flip
 359 current matrix elements required to compute $F_1(Q^2)$ and $F_2(Q^2)$, have an exact
 360 representation in terms of the overlap of the nonperturbative hadronic light-
 361 front wave functions, the eigen- solutions of the QCD light-front Hamiltonian.
 362 As well as elastic form factors, this framework is also capable of predicting
 363 hadronic transition form factors, structure functions and the mass spectra of
 364 mesons and baryons.

365 The calculations depicted in Fig. 4 [24] use three adjustable parameters to fit
 366 the available proton and neutron form factor data. Two of these give the proba-
 367 bilities of higher Fock states (pion cloud contributions) for $F_2(Q^2)$, which, from
 368 comparison with data, are 30% (proton) and 40% (neutron). Departure of the
 369 third (parameter r Fig. 4) from unity is interpreted as indicative of SU(6) spin-
 370 flavor symmetry breaking effects . The computed curves have an estimated
 371 accuracy of $\sim 10\%$, give a good account of the available G_E/G_M data for pro-
 372 tons and neutrons (with $r = 2.08$) and also describe a u/d flavor separation of
 373 F_1 and F_2 as performed in Ref. [25].

374 Note that, unlike the DSE framework, LFHQCD predicts that $\mu_n G_E^n/G_M^n$ rises
 375 towards an asymptotic value of ~ 0.85 , rather than bending over and decreasing
 376 towards zero. Such large differences in theoretical predictions emphasize the
 377 importance of collecting neutron data in the $Q^2 \sim 4 - 10 \text{ (GeV/c)}^2$ region.

378 1.2.4 The link with Generalized Parton Distributions

379 Generalized Parton Distributions (GPD) describe correlations between spatial
 380 and momentum degrees of freedom and permit the construction of various types
 381 of "3-D images" of the nucleon. The nucleon elastic form factors are critical
 382 to the experimental determination of GPDs [26]. In Deeply Virtual Compton
 383 Scattering (DVCS), which is generally held to be the optimum channel to access
 384 GPD information, the interference between Bethe Heitler and DVCS Handbag
 385 mechanisms is measured and the separation of these amplitudes requires EMFF
 386 information. The first moments of GPDs are related to the elastic form factors
 387 through model independent sum rules:

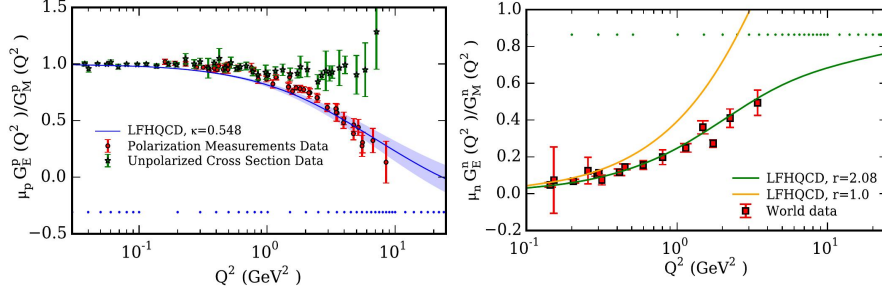


Figure 4: Predictions of Light Front Holographic QCD [24] for the ratios G_E^p/G_M^p (left) and G_E^n/G_M^n (right) .

$$\int_{-1}^{+1} dx H^q(x, \xi, Q^2) = F_1^q(Q^2) \quad \int_{-1}^{+1} dx E^q(x, \xi, Q^2) = F_2^q(Q^2) \quad (4)$$

These relations are currently some of the most important constraints on the forms of the GPD's and, since it is extremely unlikely that the GPDs will be mapped out exhaustively in the near future, constraints such as those in Eq.4 will be critical to extraction of GPD's. Already the constraints from Eq.4 have played an important role in the first estimates of nucleon quark angular momentum using the Ji Sum Rule and constraining GPDs is in itself an excellent reason to experimentally determine the nucleon elastic form factors.

1.3 Previous EMFF Measurements

1.3.1 Unpolarized

There have been many extractions of the Sachs form factors from Rosenbluth separation of unpolarized differential cross sections. Three of the more recent are given in Ref. [14, 15, 16]. A measurement of proton form factors in Hall-C [15] essentially follows the scaling trend of a previous measurement from SLAC [14]. In Hall-A a proton measurement [16] at Q^2 values of 2.64, 3.20 and 4.10 (GeV/c)² has also been made, but in this case the differential cross sections were determined by detecting the recoiling proton, in contrast to older measurements where the scattered electron was detected.

Essentially the Rosenbluth extractions all follow $\mu G_E \sim G_M$ scaling. They are in definite disagreement with recent polarization transfer measurements of comparable precision (Fig. 1), which has been attributed to the relative sensitivity of Rosenbluth separation to two-photon-exchange effects.

1.3.2 Polarized Target

Vector Polarized ²H has the neutron and proton spins aligned in parallel. At NIKHEF a polarized deuterium gas target was used to determine G_E^n at $Q^2 = 0.21$ [27] via measurement of the spin-correlation parameters. At JLab the range of Q^2 for G_E^n was extended to 0.5, 1.0 (GeV/c)² [28, 29], using a

414 polarized deuterated ammonia (ND_3) target. For neutron measurements, po-
 415 larized ^3He has the advantage that $\sim 90\%$ of the nuclear polarization is carried
 416 by the neutron. At Mainz, a series of polarized ^3He target measurements have
 417 taken place over a range of $Q^2 = 0.31 - 1.5 \text{ (GeV/c)}^2$ [30, 31, 32, 33]. In the
 418 GEN(1) experiment at JLab [6] the higher beam energy, high performance ^3He
 419 target and large acceptance detectors has enabled the Q^2 range to be extended
 420 up to 3.4 (GeV/c)^2 .

421 1.3.3 Recoil Polarimetry

422 There have been several experiments to measure G_E^n/G_M^n from the polarization
 423 of the recoiling nucleon (Sec. 2.1) after scattering of the polarized electron.
 424 Proof-of-principle measurements at MIT-Bates [34] were followed by more pre-
 425 cise measurements at Mainz. The latter firstly within collaboration A3 [35, 36]
 426 and subsequently within collaboration A1 [37]. While the Mainz program was
 427 still in progress, experiments at JLab came online, and Hall-C measurements of
 428 G_E^n/G_M^n have been published at Q^2 of 0.45, 1.13 and 1.45 (GeV/c)^2 [7], the last
 429 of which is currently the highest value of Q^2 measured by recoil polarization.

430 The beam energy at pre-upgrade JLab (6 GeV) was significantly higher than
 431 Mainz (1.6 GeV) and this has enabled JLab to take the lead in measurements
 432 of G_E^p/G_M^p [9, 10, 12, 13], which now extend to a Q^2 value of 8.5 (GeV/c)^2 . This
 433 series of measurements has shown conclusively that $\mu G_E \neq G_M$ and may suggest
 434 that the ratio crosses zero at some higher value of Q^2 . However the precision
 435 of the higher Q^2 data points is not sufficient either to pin down that crossing
 436 point or to show unambiguously that it exists. The first of these measurements
 437 [9] is the most highly cited paper ever published on a JLab experiment.

438 1.4 Related EMFF Measurements at JLab.

439 Measurement of the nucleon EMFF will be a major component of Hall-A/SBS
 440 experimental programme. The SBS project has three approved EMFF measure-
 441 ments: G_E^n/G_M^n [1], G_M^n/G_M^p [2] and G_E^p/G_M^p [3]. These three measurements,
 442 together with a very precise measurement of G_M^p [4] in Hall A using the HRS
 443 Spectrometers, will collectively determine all four nucleon form factors with un-
 444 precedented reach in Q^2 and accuracy. In Hall-C an experiment to measure
 445 G_E^n/G_M^n using the SHMS electron spectrometer and a custom built neutron po-
 446 larimeter has been approved [5] and in Hall-B there is an approved experiment
 447 to measure G_M^n/G_M^p [38].

448 1.4.1 E12-11-009: *The Neutron Electric Form Factor at Q^2 up to* 449 *7 (GeV/c)^2 from the Reaction $^2\text{H}(\vec{e}, e' \vec{n})$ via Recoil Polarimetry*

450 This measurement of G_E^n/G_M^n [5] from quasi-elastic $^2\text{H}(\vec{e}, e' \vec{n})$ has been ap-
 451 proved for Hall-C using the Super High Momentum Spectrometer (SHMS) and
 452 a custom built neutron polarimeter (NPOL). At present, the polarimeter regis-
 453 ters $n - p$ interactions in a series of segmented plastic-scintillator analyzers and
 454 detects recoiling protons in top and bottom segmented arrays of $\delta E - E$ counters.
 455 This current geometry is optimized to detect a relatively low momentum, large-
 456 angle recoiling proton after n-p scattering. The C-GEN collaboration is investi-

gating a variety of options to increase sensitivity to the charge-exchange channel within NPOL to maximize the FoM for Q^2 values beyond those of the initially approved experiment. Members of the C-GEN collaboration have joined the present proposal because of interest in understanding the analyzing power and systematics for small-angle recoiling protons from the charge-exchange channel, as well as the opportunity to study aspects of the large-angle recoiling protons within the same apparatus.

1.4.2 E12-09-016: *Measurement of the Neutron Electromagnetic Form Factor Ratio G_E^n/G_M^n at high Q^2*

This experiment [1] will measure the double-spin asymmetry in quasi-elastic $\vec{^3He}(\vec{e}, e'n)pp$ using a new highly-polarized 3He target, capable of withstanding beam currents up to $60 \mu A$. The scattered electron will be detected in BigBite and the recoiling neutron in a hadron calorimeter (HCAL). Measurements are proposed at $Q^2 = 1.5, 3.7, 6.8, 10.2$ (GeV/c) 2 , which can be compared to the current highest GEN(1) point at $Q^2 = 3.4$ (GeV/c) 2 . Accurate new G_E^n/G_M^n data at medium-high Q^2 will have enormous physics impact. Clean separation of the QE signal from inelastic background is considerably more challenging for 3He compared to 2H and nuclear-medium effects for a neutron bound in 3He will also be larger. Development of the polarized 3He target is making good progress, but never the less it will be a major challenge to maintain the predicted 60% polarization with an incident $60 \mu A$ electron beam.

Although E12-09-016 can in principle achieve superior precision to a recoil-polarimetry experiment, its systematic uncertainties will be considerably larger and confirmation of its results by recoil polarimetry, a different experimental technique, will be extremely important.

1.4.3 E12-09-019: *Precision Measurement of the Neutron Magnetic Form Factor up to $Q^2 = 13.5$ (GeV/c) 2*

In experiment E12-09-019 [2] a high precision measurements of the ratio G_M^n/G_M^p will permit the reconstruction of the individual u and d quark distributions with an impact-parameter resolution of 0.05 fm. These data are needed both to determine the $u - d$ difference and to study the QCD mechanisms which govern these distributions. G_M^n/G_M^p will be obtained from the cross-section ratio of $^2H(e, e'n)$ and $^2H(e, e'p)$ quasi-free scattering from the deuteron. This ratio method has also been proposed using CLAS12 (Sec. 1.4.6) which can measure on a fine grid of Q^2 points. However, the SBS measurement can be made at much higher luminosity and can achieve superior precision at high Q^2 . The HCAL calorimeter for the SBS measurement offers very similar proton and neutron detection efficiencies which are close to 100%. This suppresses a potential major source of systematic uncertainty in the ratio method.

The proposed apparatus for the present experiment is just the E12-09-19 apparatus, with the inclusion of the neutron polarimeter.

498 **1.4.4 E12-07-109: Large Acceptance Proton Form Factor Ratio Mea-**
499 **surements at High Q^2 using the Recoil Polarization Method**
500 **[3].**

501 This experiment will measure the ratio G_E^p/G_M^p at $Q^2 = 5, 8, 12 \text{ (GeV/c)}^2$ with
502 a relative uncertainty of ~ 0.1 , which should confirm the zero-crossing point in
503 Q^2 , if it exists. The experiment will use the 11 GeV polarized electron beam,
504 a 40 cm long liquid hydrogen target, the BigCal electromagnetic calorimeter to
505 detect the elastically scattered electrons and SBS, equipped as a polarimeter,
506 for the detection of the recoiling proton. A luminosity of $\sim 10^{39} \text{ cm}^{-2} \text{ s}^{-1}$ will
507 be necessary to reach the desired precision, and the technical solutions to the
508 problems imposed by high rates in the detectors will be of general benefit to the
509 SBS programme.

510 The present experiment will use the same GEM trackers and hadron calorimeter
511 designed originally for the E12-07-109 polarimeter.

512 **1.4.5 E12-07-108: Precision measurement of the Proton Elastic Cross**
513 **Section at High Q^2**

514 This experiment [4] used the two Hall-A HRS to perform a high precision (2-
515 4%) measurement of $H(e, e'p)$, over a range of Q^2 up to 13.5 (GeV/c)^2 . This
516 experiment ran in 2016 and the data will yield high precision values of G_M^p . The
517 original goal was to reach higher values of Q^2 , but the limited available beam
518 time curtailed the possibility to reach the highest approved Q^2 values. Never
519 the less a value of 13.5 (GeV/c)^2 is still as big as that currently approved in any
520 SBS experiment.

521 **1.4.6 E12-07-104: Measurement of the Neutron Magnetic Form Fac-**
522 **tor at High Q^2 Using the Ratio Method on Deuterium**

523 This measurement of the G_M^n/G_M^p ratio has been proposed using CLAS12 [38].
524 Compared to E12-09-019 (Sec. 1.4.3) this experiment can measure in one setting
525 a broad kinematic range on a fine grid of Q^2 points. By contrast E12-09-019
526 will measure at several discrete kinematic settings on a coarser grid, but can
527 achieve higher experimental luminosity.

528 **2 Double-Polarized Measurements of G_E/G_M**

529 The double polarization method for the measurement of G_E was originally pro-
530 posed [39] to improve the experimental sensitivity to the spin-flip form factor F_2
531 at large momentum transfer, and subsequent work [40] developed the formalism.
532 A number of form-factor measurements have been performed in recent years:
533 either with polarized nucleon targets, or with a polarimeter to measure the po-
534 larization transfer to the recoiling nucleon. The technique of choice depends
535 on the comparison of achievable luminosity, detector efficiency, detector accep-
536 tance and the experimental asymmetry, which in turn depends on the target
537 polarization or polarimeter analyzing power.

538 In the case of the neutron, quasi-elastic scattering from the neutron bound in
 539 ^2H or ^3He offers the nearest approximation to the free scattering case. Bound-
 540 nucleon and final-state-interaction effects become less important as momentum
 541 transfer increases above $\sim 1 (\text{GeV}/c)^2$ [41], but none the less the suppression of
 542 inelastic channels becomes increasingly difficult at higher Q^2 and it is highly de-
 543 sirable to have data on both targets to check consistency. Neutron measurements
 544 are inherently more challenging than their proton equivalents, as demonstrated
 545 by their more restricted kinematic range $G_E^n/G_M^n : Q^2 \leq 3.4 (\text{GeV}/c)^2$ as op-
 546 posed to $G_E^p/G_M^p : Q^2 \leq 8.5 (\text{GeV}/c)^2$. High precision measurements of G_E^n/G_M^n
 547 at $Q^2 = 4.5 (\text{GeV}/c)^2$, followed by measurements as high as $9.3 (\text{GeV}/c)^2$, will
 548 have extremely high selectivity of the quite diverse predictions of different the-
 549 oretical models. Thus it is extremely important to have reliable, independently
 550 verified neutron results.

551 Whether working with a polarized target or a recoil polarimeter, the ability
 552 to separate G_E from G_M and the relative freedom from possible two-photon
 553 exchange effects make double-polarization asymmetry measurements the tech-
 554 niques of choice for accessing G_E^n .

555 2.1 Polarized Beam and Recoil Polarimetry

556 For a free nucleon the polarization transferred from the electron to the nucleon
 557 can be written as:

$$P_x = -hP_e \frac{2\sqrt{\tau(1+\tau)} \tan \frac{\theta_e}{2} G_E G_M}{G_E^2 + \tau G_M^2 (1 + 2(1+\tau) \tan^2 \frac{\theta_e}{2})} \quad (5)$$

$$P_y = 0 \quad (6)$$

$$P_z = hP_e \frac{2\tau \sqrt{1+\tau + (1+\tau)^2 \tan^2 \frac{\theta_e}{2}} \tan \frac{\theta_e}{2} G_M^2}{G_E^2 + \tau G_M^2 (1 + 2(1+\tau) \tan^2 \frac{\theta_e}{2})} \quad (7)$$

$$\frac{P_x}{P_z} = \frac{1}{\sqrt{\tau + \tau(1+\tau) \tan^2 \frac{\theta_e}{2}}} \cdot \frac{G_E}{G_M} \quad (8)$$

558 where h and P_e are the helicity and polarization respectively of the electron
 559 beam. Eq.8 requires the measurement of the longitudinal component of the
 560 neutron polarization P_z and this must be precessed into the transverse plane.
 561 The angle of precession through a magnetic field may be expressed as

$$\chi = \frac{2\mu_n}{\hbar c} \frac{1}{\beta_n} \int_L \mathbf{B} \cdot d\mathbf{l} \quad (9)$$

562 where $L(x, y, z)$ is the path through the field, $\mathbf{B} = (B_x, B_y, B_z)$ is the flux
 563 density, μ_n is the neutron magnetic moment and β_n is the neutron velocity.
 564 With a horizontal field $(B_x, 0, 0)$ the spin will precess in the $y - z$ plane (See
 565 Sec.2.2).

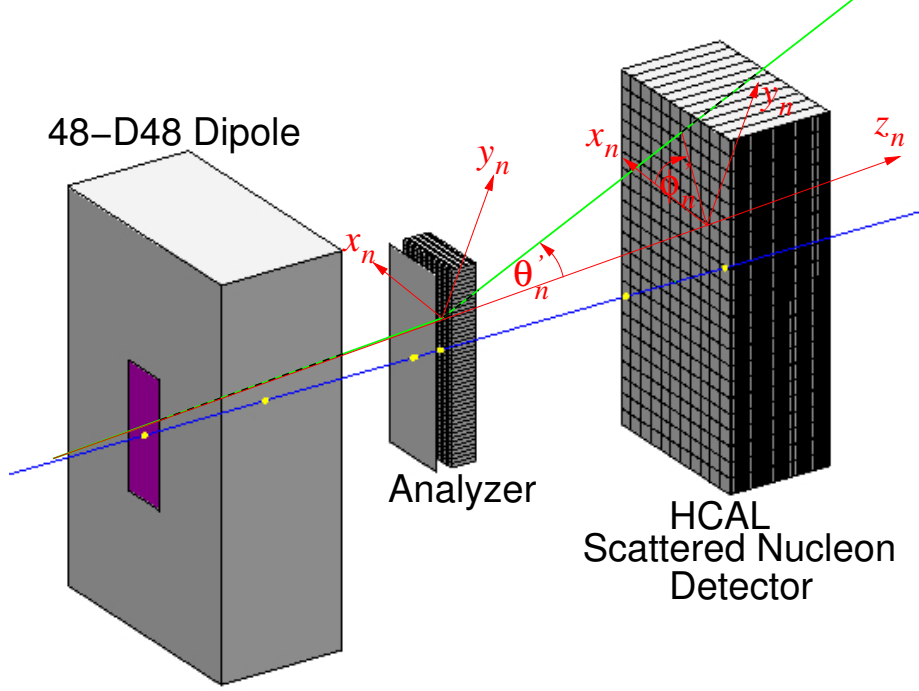


Figure 5: Schematic view of a neutron polarimeter, using SBS detector components

2.2 Nucleon Polarimetry

Nucleon polarimetry depends on the spin-orbit interaction of an incident nucleon with a target nucleon or nucleus, which produces an azimuthal modulation of the scattering cross section:

$$\sigma(\theta'_n, \phi'_n) = \sigma(\theta'_n) \left[1 + A_y(\theta'_n) \left\{ P_x^n \sin \phi'_n + P_y^n \cos \phi'_n \right\} \right] \quad (10)$$

where $\sigma(\theta'_n)$ is the unpolarized scattering differential cross section, $A_y(\theta'_n)$ is the analyzing power of the scattering process and P_x^n, P_y^n are respectively the horizontal and vertical components of the incident nucleon polarization. Scattering angles are shown in Fig.5. The effectiveness of any polarimeter will depend on a combination of its detection efficiency and analyzing power, which can be parametrized as a Figure of Merit (FoM) \mathcal{F} given by:

$$\mathcal{F}^2(p_n) = \int \varepsilon(p_n, \theta'_n) A_y^2(p_n, \theta'_n) d\theta'_n \quad (11)$$

where $\varepsilon(p_n, \theta'_n)$ is the detection efficiency which depends on the cross section for the scattering process and the thickness of the polarimeter material. The angular range is determined by the polarimeter geometry and obviously good acceptance for the region where A_y is large is important. The thickness is

usually limited in practice by multiple scattering considerations, as with multiple scattering the initial scattering plane is lost. If \mathcal{F} is known then the precision of the obtained incident polarization may be obtained from:

$$\Delta P = \sqrt{\frac{2}{N_{inc}\mathcal{F}^2}} \quad (12)$$

where N_{inc} is the number of incident particles. Note that the polarimeter proposed here (Sec. 3.2) has a large azimuthal coverage up to polar angles of $\sim 15^\circ$, which will contain most of the useful forward angle scattering. This is also advantageous for untangling the P_x and P_y polarization components.

Note that in measuring the ratio P_x/P_z (Eq.8) the analyzing power cancels, assuming that it is independent of the relative x and y components of polarization. It is however important to have a reasonable estimate of the analyzing power in order to predict the running time required to reach a given precision.

2.2.1 Neutron analyzing power at several GeV/c

Neutron polarimetry is generally based on free elastic $n-p$ scattering or elastic-like $n-p$ scattering from nuclei, where the detected proton is used to reconstruct the scattering kinematics. Elastic-like $n-n$ scattering from nuclei can also be used in principle, but in practice it is difficult or impossible to reconstruct the scattering kinematics if it is associated with a very low energy recoiling charged particle. This is necessary to select the range of polar angles where the analyzing power is relatively large (Eq.11). In comparison to proton scattering, the analyzing power A_y for neutron polarimetry at GeV energies is poorly known. Free $n-p$ scattering is in principle the best analyzer of neutron polarization, but the use of a hydrogen analyzer is challenging technically and up to now scattering from C or CH_2 has generally been used. However A_y for elastic-like scattering from nuclei is lower than the free-scattering case.

In the following the available experimental evidence (Sec. 2.2.2) is presented.

2.2.2 Experimental data for polarized nucleon-nucleon scattering

Information on polarized nucleon scattering for incident momenta $p_N \gtrsim 1.5$ GeV/c is presented in Fig. 7 A. This comes from a number of sources.

1. Measurements of the asymmetries of the $d(\vec{p}, p')n$ and $d(\vec{p}, n)p$ processes have been performed in the 1970s [43, 44] which, in the case of the former, are consistent with elastic $\vec{p} + p \rightarrow p + p$ measurements [45]. These experiments measured both $p-p$ and $p-n$ scattering.
2. Inclusive measurements of $\vec{p} + CH_2 \rightarrow p + X$ [46], and $\vec{p} + C \rightarrow p + X$ [47, 48] have been obtained in the calibration of proton polarimeters used at ANL, JINR Dubna and JLab.
3. Measurements of the asymmetries of polarized charge exchange $n + \vec{p} \rightarrow p + X$ scattering [49, 50], have also been made at ANL in the 1970s.

- 617 4. A measurement of polarized charge-exchange $\vec{n} + A \rightarrow p + X$ [51] has been
 618 made for C, CH, CH₂ and Cu targets at incident momenta ~ 4 GeV/c in
 619 November 2016 and February 2017 at JINR Dubna (Sec. 7).

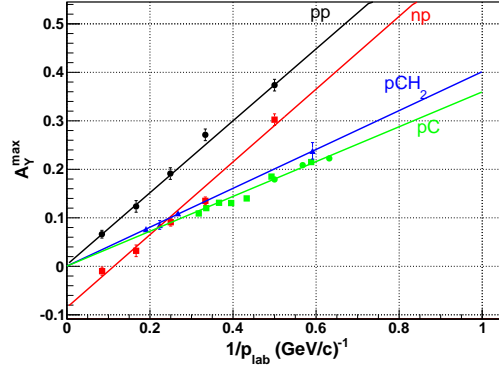


Figure 6: The dependence of the maximum of A_Y on $1/p_{lab}$. Black circles: ANL $d(\vec{p}, p')n$ data [43, 44]; black line: linear fit. Red squares: ANL $d(\vec{p}, n)p$ data [43, 44]; red line: linear fit. Blue triangles [46]: $\vec{p} + \text{CH}_2 \rightarrow \text{charged} + X$; blue line: linear fit [46]. Green squares [47] and circles [48]: $\vec{p} + \text{C} \rightarrow \text{charged} + X$; green line: linear fit [46].

620 Fig.6 displays the maximum values of the angle-dependent polarization asym-
 621 metries of $p-p$ and $p-n$ scattering, as determined from the data of Ref.[43, 44,
 622 46, 47, 48] and plotted in as a function of $1/p_{lab}$. The main features include the
 623 negative offset of the $p-n$ data with respect to $p-p$. The factor 2 reduction
 624 in the analyzing power of quasi-free (^{12}C) with respect to free $p-p$ scattering
 625 is presumably similar for $n-p$ scattering, but to our knowledge there are no
 626 data on polarized $n-p$ scattering from nuclei in the multi-GeV energy domain.
 627 From (Fig. 7 top) it is evident that $p-n$ (equivalent to $n-p$) polarization
 628 is dependent on incident nucleon momentum p_{lab} , as well as t , where $-t$ is
 629 the squared four-momentum transfer. On the other hand charge-exchange $n-p$
 630 (Fig. 7 Bottom) is t -dependent, with a large polarization at sufficiently large $-t$,
 631 but given the spread in the data there is no apparent strong dependence of A_y
 632 on p_{lab} . New polarized, charge-exchange data from JINR Dubna [51] (Sec. 7)
 633 also show a sizable asymmetry, but an assessment of the reduction factor in
 634 analyzing power, compared to the free-scattering case, awaits a more detailed
 635 analysis.

636 2.2.3 The Figure of Merit for neutron polarimetry

637 Neutron-polarimeter FoM values (Eq. 11) have been calculated over a range of
 638 p_{lab} for both charge-exchange $n-p$ and $n-p$ scattering.

639 Elastic-like $p-p$ scattering from nuclei is observed to have a factor-two reduction
 640 in A_Y compared to the free elastic $p-p$. For $n-p$, an application of the same
 641 reduction factor is consistent with the polarimeter analyzing power obtained in
 642 a previous JLab measurement of G_E^n/G_M^n [7] at 1.45 GeV/c. The value of A_y

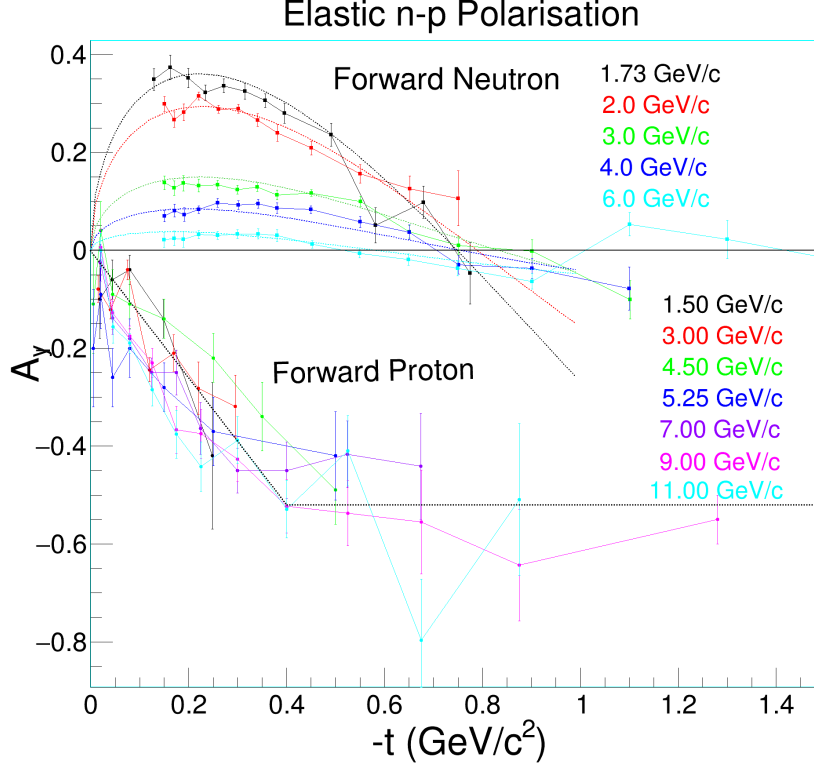


Figure 7: Top: the p_{lab} and t -dependence of the polarization of $p - n$ scattering [43, 44]. The smooth dotted lines show the fit of Ref. [52] to the $p - n$ data. Bottom: the p_{lab} and t dependence of charge-exchange $n - p$ scattering [49, 50]. The color coding relates the data to momentum labels.

for free, elastic $n - p$ scattering has been calculated from a fit [52] (Fig. 7) to the $p - n$ data. For charge-exchange $n - p$ scattering from Cu, A_y is taken from a preliminary analysis of new data from Dubna (Sec. 7). This analysis has given the dependence of A_y on $p_t = p_{lab} \sin \theta_{np}$ at an incident momentum of 3.75 GeV/c. A_y is dependent on p_t , but has been assumed independent of p_{lab} , in a manner consistent with the free charge-exchange $n - p$ data (Fig. 7). Polarimeter efficiencies have been calculated using Monte Carlo (MC) simulations of the polarimeter which record the differential detection efficiency as a function of scattering angle. The MC generated data have been filtered according to cuts on energy and angle (Sec. 4.3). Calculations have been made for two versions of the polarimeter compatible with the SBS apparatus.

1. The polarimeter uses the proposed Cu analyzer with forward-angle proton detection by GEM trackers and hadron calorimeter.
2. The polarimeter employs an active position sensitive CH (plastic-scintillator) analyzer with forward angle neutron detection by the hadron calorimeter.

At neutron momenta above ~ 3.5 GeV/c, the FoM from charge-exchange $n - p$ starts to dominate standard $n - p$ and by ~ 6 GeV/c it is projected to be a factor ~ 15 larger. The present experiment will verify if these projections are accurate at $p_n = 3.15$ GeV/c and allow for a real-world evaluation of systematics associated with using the charge-exchange channel to extract G_E^n at $Q^2 = 4.5$ (GeV/c) 2 and beyond.

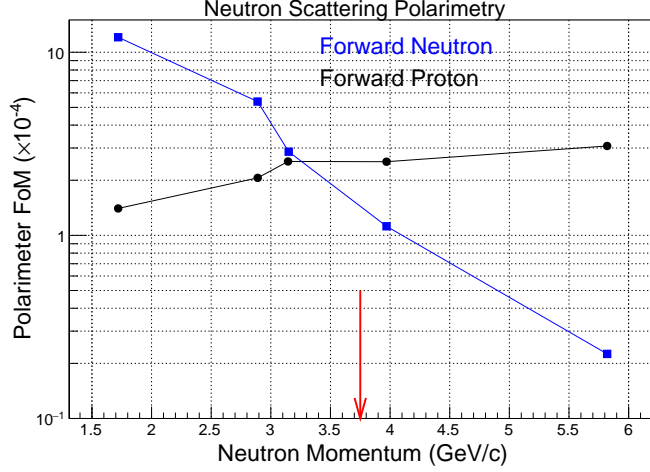


Figure 8: Neutron polarimeter figure of merit as a function of incident neutron momentum for two styles of polarimeter within the SBS apparatus using preliminary data from the recent Dubna measurement. Blue squares: standard $n - p$ scattering from CH scintillator, black circles: charge-exchange $n - p$ scattering from Cu. The red arrow marks the neutron momentum at which a charge-exchange measurement of the analyzing power of Cu was made at Dubna.

3 Experimental Method

The recoil polarization technique requires a large number of counts, because of the relatively low analyzing power of the polarimeter. Going to high momentum transfer, where the elastic scattering rate scales approximately as E_{beam}^2/Q^{12} , requires high luminosity, large acceptance and a high rate capability in the detection system. A plan view of the detector apparatus is displayed in Fig.9.

Almost all of the detectors of the present proposal are already under construction for other SBS experiments. Most of the apparatus is identical to that used in the approved G_M^n/G_M^p experiment E12-09-019, which will undergo a JLab “Readiness Review” in June 2017.

- The same LD_2 target and beam line is used.
- The luminosity at $1.25 \times 10^{38} \text{ cm}^{-2} \text{ s}^{-1}$ is the same.
- The same BigBite spectrometer on the e’ arm is used and the configuration of the detector is identical.

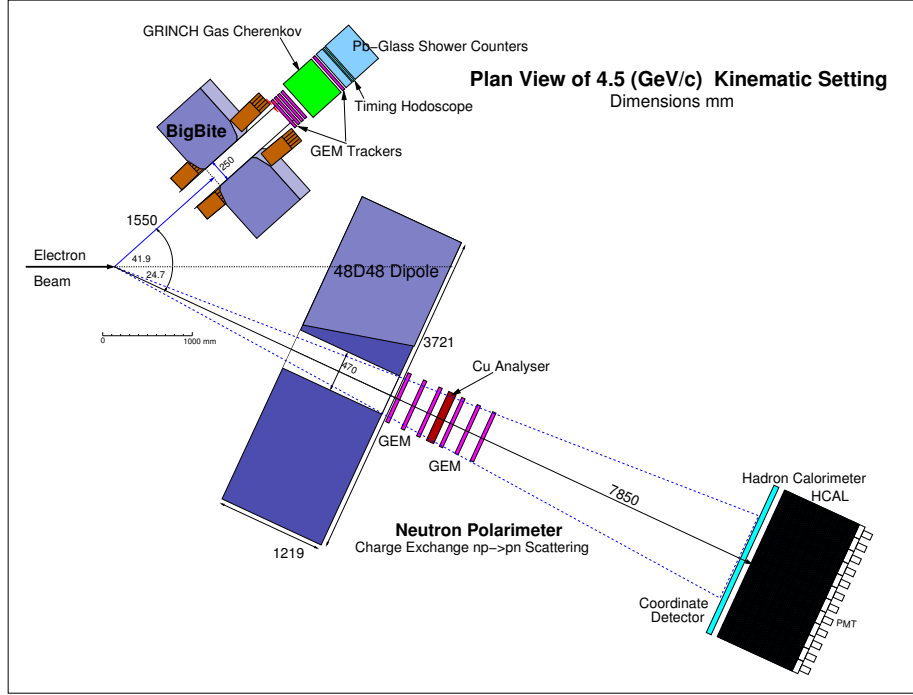


Figure 9: Plan view of experiment $Q^2 = 4.5 \text{ (GeV/c)}^2$.

- The same 48D48 dipole on the hadron arm is used.
- The same HCAL hadron calorimeter is employed for the detection of energetic protons and neutrons.
- The same CDet coordinate detector is used in front of HCAL for additional particle and position identification.

G_{En}/G_{Mn} experiment E12-09-016 will also use the detectors and dipole itemized above. The additional GEM tracking detectors for the present neutron polarimeter are also used in the proton polarimeter of G_E^p/G_M^p experiment E12-07-109, but the Cu analyzer block and additional large-angle proton detectors will be new.

We propose to perform the measurement in Hall-A of Jefferson Laboratory, using the CW, polarized electron beam from the CEBAF accelerator. This has a maximum energy of 11 GeV and maximum current of $80 \mu\text{A}$. The present experiment will use a beam energy of 4.4 GeV (Table 3) an integral factor of a the standard 2.2 GeV energy gain per pass around the race track. Beam polarizations in excess of 80% have been achieved routinely during 6 GeV operation of CEBAF and 80% is assumed for estimates of precision in measuring form factor ratios.

The electrons will be incident on a 10 cm long liquid deuterium (LD_2) target with $100 \mu\text{m}$ Al entrance and exit windows, giving $\sim 0.054 \text{ g/cm}^2$ of material, compared to $\sim 1.69 \text{ g/cm}^2$ for the LD_2 . A liquid hydrogen (LH_2) target will

700 also be used for calibrations. A 40 μA electron beam incident on a 10 cm LD_2
 701 target produces an electron-neutron luminosity of $\sim 1.26 \times 10^{38} \text{ cm}^{-2}\text{s}^{-1}$.
 702 Scattered electrons are detected in the BigBite spectrometer, which will re-
 703 construct the momentum, direction and reaction vertex, as well as correlating
 704 the trigger time to an accelerator beam bunch. The neutron arm will be a po-
 705 larimeter which consists of a Cu analyzer, preceded and followed by sets of GEM
 706 trackers, and the hadron calorimeter HCAL. The polarimeter will provide posi-
 707 tion and time-of-flight information for the recoiling nucleon, as well as scattering
 708 asymmetries. Neutron spin precession will be performed by the “48D48” dipole
 709 which is the basis of the SBS charged-particle spectrometer. The experimental
 710 components are described in more detail in the following subsections.

711 3.1 The e' Spectrometer BigBite

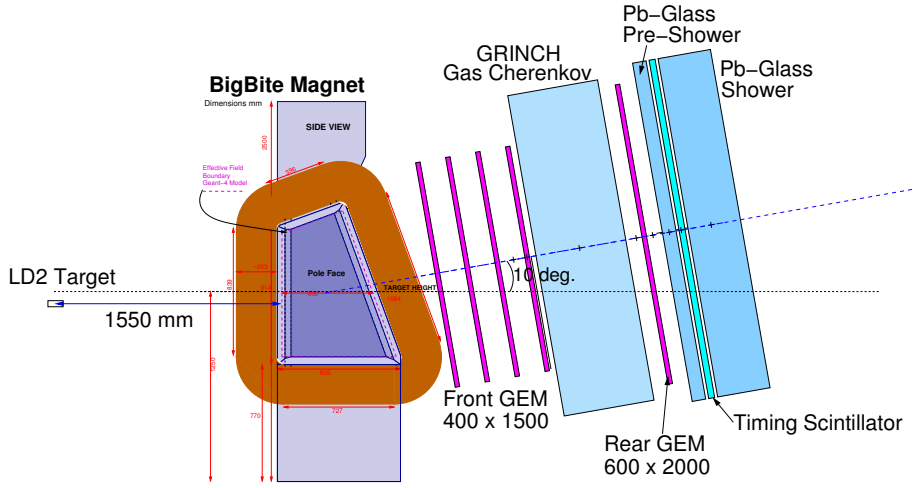


Figure 10: The BigBite electron spectrometer

712 BigBite is a large-acceptance, non-focusing magnetic spectrometer which, when
 713 positioned with the entrance aperture of the dipole 1.55 m from the target center,
 714 subtends a solid angle of $\sim 58 \text{ msr}$. The configuration of BigBite for the present
 715 experiment would be identical to that of experiment E12-09-019 to measure
 716 G_M^n/G_M^p and experiment E12-09-016 to measure G_E^n/G_M^n . The components of
 717 BigBite are described in the following.

718 3.1.1 Dipole Magnet

719 The 20 ton dipole, constructed at the Budker institute, was used originally at
 720 NIKHEF and has been used in several experiments performed with the 6 GeV
 721 CEBAF accelerator. With the entrance aperture at 155 cm from the target
 722 center, the minimum central scattering angle that BigBite can reach (limited by
 723 the proximity of the exit beam line) is around 30 deg. The maximum integrated
 724 field is 1.2 Tm, so that for GeV electrons the bend angle is relatively small,
 725 approximated by:

$$\theta_e \approx \frac{0.3 \int B \cdot dl}{p_e} \quad (13)$$

where the field integral is in Tm and the electron momentum in GeV/c. The angular uncertainty of the deflected electrons from the coordinate resolution of the tracker, taking multiple Coulomb scattering into account, may be estimated for relativistic electrons as

$$\delta\theta = \sqrt{\left(\frac{\sigma_r}{z_{tr}}\right)^2 + \left(\frac{13.6}{p_e} \sqrt{\frac{x}{X_0}} \left[1 + 0.038 \ln\left(\frac{x}{X_0}\right)\right]\right)^2} \quad (14)$$

where p_e is the electron momentum in MeV/c and x/X_0 is the thickness of intervening material in radiation lengths. The materials in the front tracking system (Sec.3.1.2) amount to $x/X_0 \sim 0.017$ and the angular uncertainty from the tracking coordinate resolution is ~ 0.5 mr. This translates to an angular resolution of (in both dispersive and non-dispersive directions) of $\delta\theta \sim 1.4$ mr at $p_e = 1.14$ GeV/c and $\delta\theta \sim 0.6$ mr at $p_e = 3.81$ GeV/c.

The momentum resolution $\delta p/p \sim 0.5\%$ will be adequate to identify quasi-elastic scattering in the present experiment (Sec.4.7). The z-vertex resolution at the target is around ~ 2 mm. It is extremely important to have an accurate knowledge of the vertex and direction of the virtual photon, so that the BigBite optics and vertex reconstruction will be calibrated at each kinematic setting, using a sieve slit and multi-carbon-foil target. Momentum will be calibrated using elastic $e - p$ scattering from a LH_2 target.

3.1.2 Front and Rear GEM Trackers

The GEM trackers supersede the MWDC, used in experiments during the 6 GeV CEBAF era, and offer increased counting rate capability, so that higher experimental luminosities may be achieved.

The front GEM trackers are under construction at INFN Rome (Sanita). They are based on triple-foil GEM modules each 40×50 cm in area, grouped in threes to give an area of 40×150 cm per tracking plane. The 2D readout strips are pitched at 0.4 mm which give a coordinate resolution of 0.070 mm. Readout of the strips is performed by the APV25 ASIC which records the strip charge at a sampling rate of 40 MHz (25 ns per sample) and the start time can be reconstructed to ~ 5 ns precision.

The rear GEM tracker is under construction at The University of Virginia (UVa). It is similar to the front GEMs, but each module is 60×50 cm in area and the single plane will be constructed from 4 modules to give an area of 60×200 cm. The pitch of the readout strips is the same as for the front GEMs, so that these planes will also have a coordinate resolution of ~ 0.07 mm. Readout of the strips will also be by the APV25 chip.

Front and rear trackers will be separated by the GRINCH gas Cherenkov counter.

3.1.3 GRINCH Gas Cherenkov

Separation of e^- from π^- particles will be performed by the “GRINCH” gas Cherenkov counter which being constructed at The College of William and Mary

(W&M). Light is collected by four cylindrical mirrors and reflected on to a set of 510 9125 PMT's, which have a diameter of 29 mm. Compared to the previous BigBite gas Cherenkov, which used 130 mm PMTs, the new detector will have superior counting rate capability and will be much less susceptible to soft background from the electron beam line. Photons produced by electron tracks through the gas will produce clusters of hits in adjacent PMTs which will be identified by time coincidence. Work is in progress to include GRINCH signals in the BigBite trigger. By suppressing events from non-electron charged particles and energetic photons from π^0 decay the experimental trigger rate will be reduced considerably (Sec. 4.6). The chamber will operate at just above 1 atm pressure and the standard gas will likely be C_4F_{10} ($\eta = 1.0015$), which has a π^- threshold of ~ 2.5 GeV/c at 1 atm, but CO_2 ($\eta = 1.00045$), would also be possible for higher momentum operation, giving a π^- threshold of ~ 4.6 GeV/c

3.1.4 Timing Hodoscope

Timing from BigBite is provided by a plastic scintillator hodoscope. For high luminosity operation a new, finer granularity, hodoscope is being constructed by The University of Glasgow (UGla). This will consist of 90 EJ200 plastic scintillator bars, dimensions $25 \times 25 \times 600$ mm, each read out by 2, ET9142 29 mm photomultipliers (PMT). The intrinsic timing resolution of this device, measured with cosmic-ray muons, is 0.15 ns, which will allow correlation with single RF beam bucket from the CEBAF accelerator, which operates at 750 MHz.

3.1.5 Pb-Glass Calorimeter

BigBite is equipped with lead glass Cherenkov pre-shower and shower counters to provide a trigger which is insensitive to low energy background, but has a high efficiency for the electrons of interest. They are the same detectors used with BigBite for 6 GeV experiments. The pre-shower counter are oriented with their long axes perpendicular the electron direction and correlation of their signal amplitude with that from the shower counters provides an additional means to distinguish electrons from π^- .

3.2 The Neutron Polarimeter

The neutron polarimeter (Fig. 9) consists of five main components:

1. The 48D48 dipole magnet
2. A $60 \times 200 \times 4$ cm block of Cu to act as the polarization analyzer.
3. Three 60x200 cm GEM chambers situated in front of the analyzer to detect and momentum analyze protons produced in the deuterium target.
4. Three 60x200 cm GEM chambers situated after the analyzer to detect and track protons produced by n-p charge-exchange, or $p-p$ scattering in the analyzer.
5. The segmented hadron calorimeter HCAL, which is optimized to detect nucleons with momenta of 1.5 - 10 GeV/c with high efficiency.

- 804 6. The coordinate detector situated immediately in front of HCAL to aid
805 particle identification and HCAL proton hit-position determination
- 806 7. The large angle proton detector

807 3.2.1 The Cu Analyzer

Material	Z	A	ρ (g/cm^3)	ρ_p (N_A/cm^3)
C	6	12.00	2.26	1.13
Al	13	26.98	2.70	1.30
Fe	26	55.85	7.87	3.22
Cu	29	63.55	8.96	4.09
W	74	183.85	19.30	7.76
Pb	82	207.19	11.35	4.49

Table 1: Comparison of the “proton density” ρ_p of common structural materials, where N_A is the Avogadro constant.

808 Cu has been chosen as the analyzer material as it has a high number of protons
809 per unit volume, which enables reasonable polarimeter efficiency to be obtained
810 with a 4 cm thick analyzer block. By contrast a C or CH_2 would be much
811 thicker to achieve similar efficiency. A thin analyzer gives more accurate kinematic
812 reconstruction of the neutron interaction position, through tracking of the
813 protons produced after charge-exchange $n-p$ scattering. Of the commonly used
814 structural materials, W has the highest proton density, but Cu has been chosen
815 as there is new empirical evidence of the analyzing power of the charge-exchange
816 $n-p$ scattering process. Although on preliminary evidence the analyzing powers
817 of C and Cu are similar (Sec.7), there is no data to show that this insensitivity
818 to Z extends to heavy nuclei. Large area Cu sheet is also more readily available
819 and cheaper than bulk W material.

820 3.2.2 The GEM Charged Particle Tracker

821 The analyzer is preceded and followed by two GEM tracking systems, each
822 consisting of 3 planes of 60×200 cm area. These detectors, which have a
823 coordinate resolution of 0.07 mm, are identical to the GEM plane which forms
824 the rear tracker of BigBite (Sec. 3.1.2). They also form the tracking system
825 for the proton polarimeter of experiment E12-07-109. The front set of GEM
826 chambers identifies protons produced in the deuterium target, while the rear
827 set identifies protons from charge-exchange $n-p$ and $p-p$ scattering in the
828 analyzer. While $n-p$ scattering is of primary interest to this proposal, the
829 ability to record $p-p$ scattering also provides the potential to measure a proton
830 asymmetry.

831 With a charged track on either side of the analyzer, the accuracy of the re-
832 construction of the hit position at the analyzer, on the basis of the exit track
833 only (as will be the case for charge-exchange $n-p$), can be checked. The cor-
834 relation of the quasi-elastic proton direction with the virtual photon direction,
835 given by BigBite on the electron arm, can also be measured directly and will

test the assumptions made for the neutron case where the direction is obtained indirectly.

If a proton scattering asymmetry can be measured with reasonable precision, this will yield a value G_{Ep}/G_{Mp} from quasi-elastic ${}^2H(\vec{e}, e'\vec{p})$. If sufficient precision is obtainable, this can be compared to the free $p(e, e'p)$ case (E12-07-109). A more quantitative assessment of proton polarimetry capability is in progress.

With both sets of trackers in place, the separation of incident neutrons from protons will be extremely positive. This will rely not only on the production of signal in the GEM chambers, but also on the reconstructed hit position at the analyzer, as protons will be deflected vertically by the dipole.

The GEM detectors have initially been designed for the G_{Ep}/G_{Mp} experiment E12-07-109 which will run an 80 μ A electron beam on a 40 cm hydrogen target. Thus they require to have a very high counting rate capability. Compared to E12-07-109, the present experiment will run at a factor ~ 8 lower luminosity and the polarimeter will sit at more backward angles. Thus we anticipate that the GEM chambers will operate comfortably in the present experiment. Detector rates are discussed in Sec.5.

3.2.3 The HCAL Hadron Calorimeter

Downstream of the tracker comes a 12×24 array of $15 \times 15 \times 90.8$ cm calorimeter modules (HCAL) which are formed from a stack of 80 alternating Fe and plastic scintillator plates. The total thickness of Fe is 50.8 cm and plastic scintillator 40 cm. HCAL will weigh around 40 tons and is under construction at CMU. Scintillation light is collected on a wavelength-shifting guide and then piped to a PMT. The time resolution for protons is expected to be ~ 0.5 ns and a resolution of ~ 0.3 ns has been measured for cosmic-ray muons. The response of HCAL to protons and neutrons will be very similar and detection efficiencies as high as 90% are expected, dependent somewhat on the applied energy threshold.

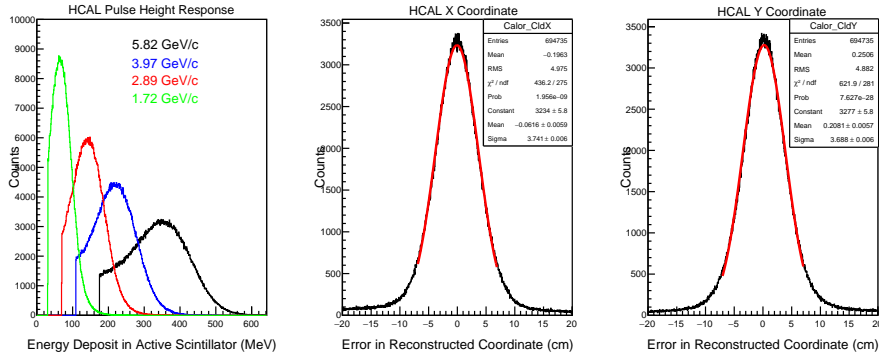


Figure 11: MC calculations of the HCAL response. **Left:** pulse height response for neutron momenta of 1.72, 2.89, 3.97 and 5.82 GeV/c; **middle:** the error in the reconstructed x-coordinate; **right:** the error in the reconstructed y-coordinate.

The simulated response of HCAL is displayed in Fig. 11 for neutrons incident on the polarimeter. Note that the Cu analyzer is in position so that HCAL

is detecting both neutrons and protons. The peaked pulse-height response, resulting from the energy deposited in the scintillator sheets, enables thresholds to be set high to remove low energy background from the experimental trigger. The threshold cuts displayed in Fig. 11 correspond to half the peak channel of the distribution. With these cuts the percentage of incident nucleons that register a hit in HCAL is $\sim 70\%$.

The response has been calculated from an energy-weighted hit cluster analysis, which also gives a hit position. The differences between the reconstructed positions and the actual hit positions (recorded in the MC data stream) is displayed in the middle and right panels of Fig. 11. The widths (σ) of these distributions are ~ 3.7 cm. Note that GEM chambers, rather than HCAL, will provide the primary information on the scattered proton direction. However the position sensitivity of HCAL will provide a useful correlation with the GEM track and the CDet position.

3.2.4 Rear Detector for Charged-Particle Identification

A “Coordinate Detector” (CDet) will sit immediately in front of HCAL to provide additional particle identification and hit coordinate information. It is under construction at JLab by Christopher Newport University (CNU) and is based on $0.5 \times 4.0 \times 51.0$ cm plastic scintillator strips arranged in modules of 392 elements. A total of 6 modules will give an area of 204×294 cm. Scintillation light produced in a strip is collected on a 2 mm diameter fast, wavelength shifting fiber and then transported to a multi-anode PMT. High-sensitivity front-end electronics, similar to those used on the GRINCH gas Cherenkov (Sec.3.1.3), will provide signals for recording of pulse charge and time. CDet is projected to have a coordinate resolution of 2 mm, a time resolution of 0.8 ns and a proton detection efficiency of 95%. It will also be used in the G_E^p/G_M^p experiment E12-07-109, the G_E^n/G_M^n experiment E12-09-016 and the G_M^n/G_M^p experiment E12-09-019. In the last two cases its placement, immediately in front of HCAL, will be identical to that proposed here.

3.2.5 Large-Angle Proton Detection

In addition to the primary goal of studying the charge-exchange channel for recoil polarimetry, there is also the potential to extract valuable information on the large-angle proton scattering channel. To this end, two active-analyzer, scintillator bars will be placed in vertical orientation near the left and right ends of the copper analyzer. The GEM planes before the analyzer will provide charged-particle identification for vetoing in software. Recoil protons emitted at large angles from n - p quasielastic scattering will be tracked by the GEM planes behind the analyzer and this tracking will be extended using additional GEM planes of the same type as in Sec. 3.2.2. They will be placed in the shielded areas along the left and right edges, outside of the flux of primary neutrons produced in the target. Additional scintillator planes will be placed downstream of the GEMs, along the large-angle tracks in the left and right regions, also shielded by the 48D48 yoke from direct view of the target. These will provide precise timing information.

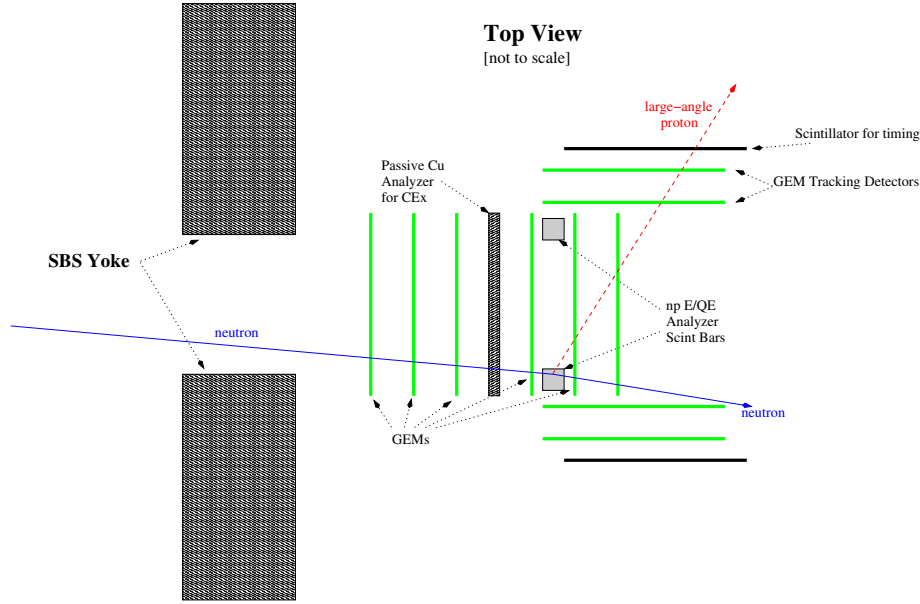


Figure 12: Preliminary schematic of the systems which enable large-angle proton detection within the SBS polarimeter.

Figure 12 shows a preliminary conceptual layout. Simulations of the acceptance and figure merit are being developed.

3.2.6 The 48D48 Dipole

For neutron polarimetry the dipole (known as 48D48) has no direct use as a spectrometer, but it serves several purposes:

1. To precess the longitudinal component of spin of the recoiling neutron to the vertical direction as the nucleon polarimeter measures transverse components of spin only.
2. To analyze the momenta of protons produced in quasi-elastic ${}^2\text{H}(e, e'p)$, which in principle can yield information on G_E^p/G_M^p derived in quasi-elastic scattering. Detection of the protons will also separate them from neutrons and further separation will be achieved through angular correlations (after proton deflection) with the \vec{q} vector of the virtual photon, determined from the electron arm.
3. To sweep low-momentum, charged background out of the acceptance of the polarimeter. For an integrated field strength of ~ 1.7 Tm, all charged particles with momenta below ~ 1 GeV/c are swept beyond the acceptance of HCAL.

The dipole is currently being modified at JLab with new coils and a slot cut in the return yoke to provide space for the exit beam line when the spectrometer is moved to forward angles.

931 4 Monte Carlo Simulations of the Polarimeter

932 4.1 Neutron Spin Precession

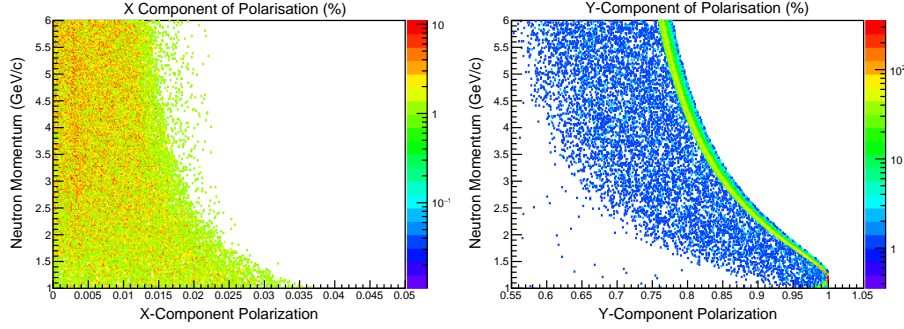


Figure 13: Neutron spin precession as a function of neutron momentum for an initial polarization (0,0,1). Left: induced values of P_x . Right: induced values of P_y .

933 Neutron spin precession through the dipole field has been calculated using the
 934 Geant-4 polarimeter model. Non-perpendicular incidence with respect to the
 935 field direction, due to fringe fields and a finite angular range, produces small
 936 rotations in the $z-x$ plane which can distort the ratio P_x/P_z and hence G_E/G_M .

937 The 48D48 dipole, is currently being modified for use in Hall A, and thus a
 938 field measurement is not yet available. However, we have calculated the size of
 939 possible $z-x$ mixing effects using field maps obtained using the 3D code TOSCA
 940 [53]. The employed field map calculation did not include any field clamps and
 941 thus probably over estimates the amount of stray field, which extends beyond the
 942 confines of the dipole aperture. At a coil excitation of ~ 2000 A, an integrated
 943 field strength of ~ 1.7 Tm is calculated, which produces a spin rotation $z \rightarrow y$
 944 (Fig.13). Neutrons with an initial polarization $\mathbf{P} = (0, 0, 1)$ and momenta of 1 -
 945 6 GeV/c were tracked through the dipole field and their polarization recorded
 946 when they impinge on the analyzer. The value of P_x , calculated after the neutron
 947 has passed through the dipole, is at the few % level. P_y values range from ~ 1
 948 at lower momenta, falling to ~ 0.75 at 6 MeV/c. Events off the main locus of
 949 the neutron momentum versus P_y curve are due to edge effects at the dipole
 950 aperture.

951 Fig.14 shows the variation of P_x and P_y over the incident coordinate at the
 952 analyzer at a neutron momentum of 3 GeV/c. Apart from events where the
 953 neutron is at the edge of the dipole aperture, P_x and P_y vary smoothly as a
 954 function of the hit position. If the maximum degree of spin transfer $z \rightarrow x$
 955 is ~ 0.03 and the expected ratio P_x/P_z in a G_E^n/G_M^n measurement is ~ 0.2 ,
 956 then the maximum error induced in a measurement of P_x/P_z will be $\sim 15\%$.
 957 However given that the hit coordinate at the analyzer can be reconstructed to
 958 < 1 cm, and the maximum gradient $\delta P_x/\delta x$ is $\sim 0.002/cm$, the maximum error
 959 after correction will be $\sim 1\%$. The size of the effect, integrated over the angular
 960 acceptance of the SBS dipole, will be smaller.

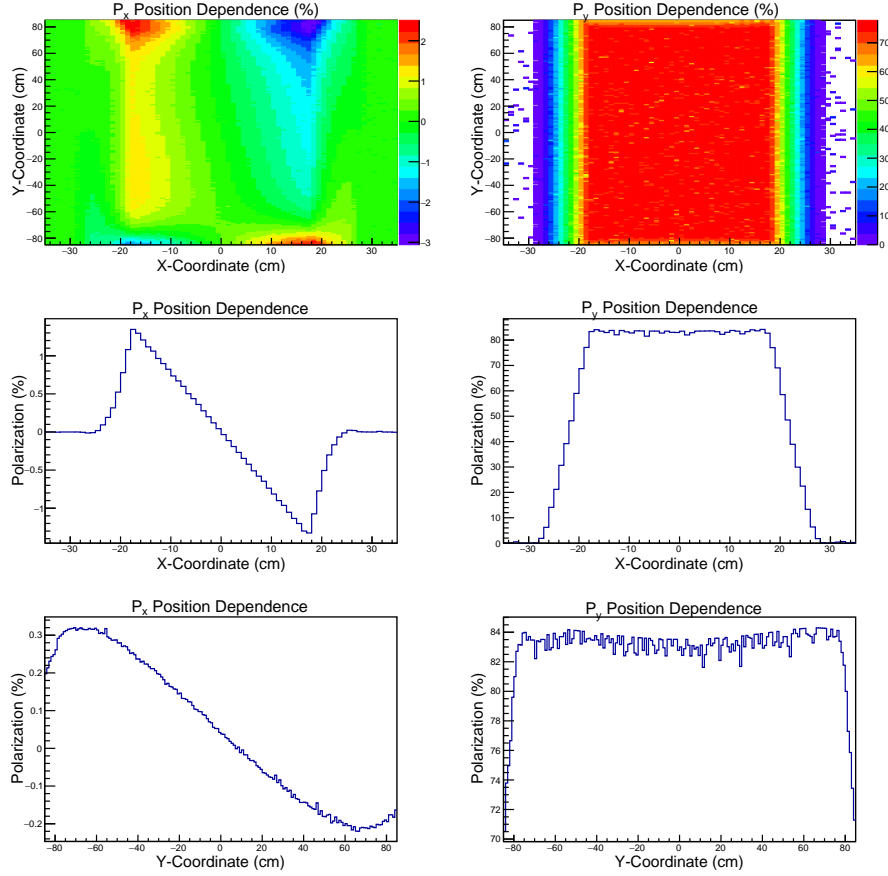


Figure 14: Neutron spin precession, variation with hit coordinate at front face of polarimeter

961 4.2 Separation of neutrons from protons

962 The present polarimeter will have a set of GEM trackers situated before the
 963 analyzer block, which will provide the primary identification and momentum
 964 analysis of protons produced in the target. Protons will be deflected by the
 965 48D48 dipole, while neutrons will not, and correlation of the nucleon direction
 966 with the virtual photon direction given by the electron arm provides a secondary
 967 means of separation.

968 Fig. 15 displays the separation of the reconstructed out-of-plane (OOP) coord-
 969 inate for neutrons and protons at the analyzer, after the protons have been
 970 deflected by the 2 Tm integrated field of the 48D48 dipole. The reconstruction
 971 procedure is described in Sec. 4.3. Equal numbers of 5.82 GeV/c neutrons
 972 and protons were incident on the analyzer, but the neutron signal is smaller as
 973 detection relies on CE $n - p$ scattering. The widths of the distributions arise
 974 dominantly from Fermi smearing of the quasi-elastic $d(e, e'N)$ process, but de-
 975 tector resolution effects are included. If a neutron-proton cut is set at an OOP
 976 position of 5 cm, then there is a 10% contamination of the neutron signal by

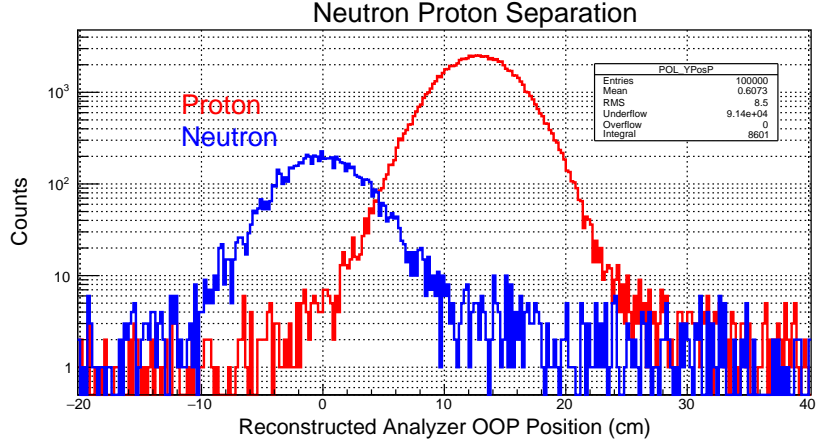


Figure 15: Separation of deflected and undeflected protons/neutrons at the Analyzer, reconstructed from the exit GEM trackers

977 protons. However protons will also be detected by the front set of GEM trackers.
 978 If this has an efficiency of 95% then the proton contamination of the neutron
 979 signal is reduced to $\sim 0.5\%$. At lower Q^2 kinematic settings, Fermi smearing will
 980 increase the widths of the distributions, but the lower momentum protons will
 981 be deflected by a larger amount so that the degree of overlap remains similar.

982 4.3 Polarimeter Angle Reconstruction

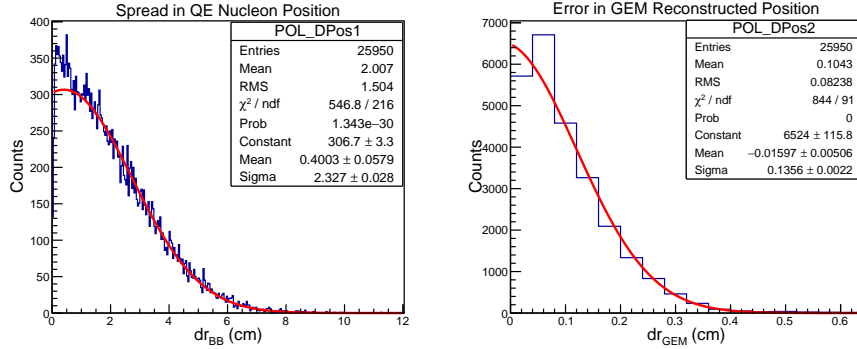


Figure 16: Reconstructed hit coordinate at the Analyzer at incident neutron momentum 5.82 GeV/c

983 Analysis of the polarimeter response involves reconstruction of the hits in the
 984 Analyzer and HCAL, followed by reconstruction of the polar and azimuthal
 985 components of the scattering angle. The scattering asymmetry is then obtained
 986 from $\sin \phi$ or $\cos \phi$ fits to the azimuthal distribution (Sec. 4.4). Any unpolarized
 987 variation in azimuthal acceptance is subtracted before the fit is made.

988 The present polarimeter is designed to detect protons produced after charge-

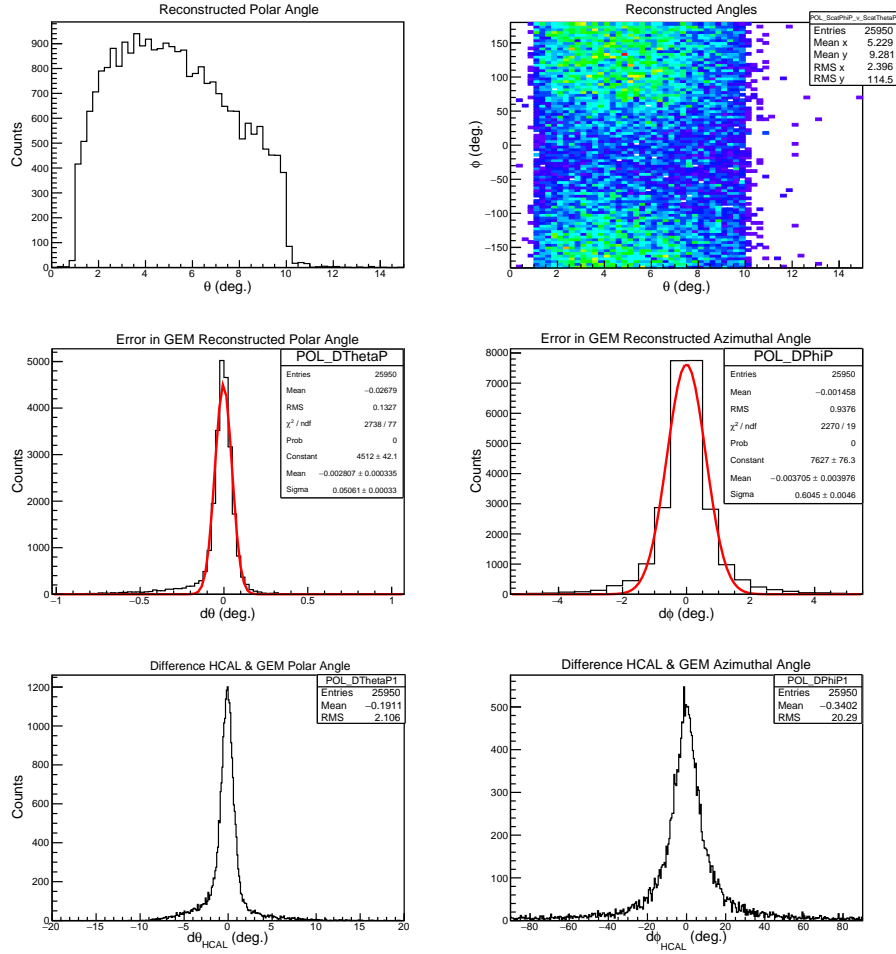


Figure 17: Polarimeter angle reconstruction at incident neutron momentum 5.82 GeV/c. The analysis has selected polar angles in the range $1.0 < \theta < 10^\circ$.

exchange neutron scattering in the analyzer material. Quasi-elastic electron scattering from the deuteron will produce both protons and neutrons incident on the polarimeter, which will also detect $p - p$ scattering. The analyzer is inert so that the direction of the exiting proton is determined using the 3 GEM chambers situated after the analyzer (Fig.9). These have a coordinate resolution of ~ 0.07 mm. Additional position information is given by CDet, which sits immediately in front of HCAL, and has a coordinate resolution of ~ 2 mm. HCAL selects high momentum protons (Fig. 11) and has a coordinate resolution of ~ 4 cm so that a cluster of hits in the calorimeter modules can be correlated with a proton track.

Fig. 16 displays the reconstruction of the neutron interaction position at the Analyzer. The left panel shows the spread in position from that expected from the virtual photon direction given by BigBite. The spread is due mainly to the Fermi motion of the nucleon in the deuteron. The right panel shows the

1003 difference in position, projected on to the plane through the center of the ana-
 1004 lyzer, between the actual hit coordinate and that reconstructed from the GEM
 1005 tracker. Fig. 17 displays the scattering angle reconstruction by the polarime-
 1006 ter for an incident neutron momentum of 5.82 GeV/c. The top panels show
 1007 the polar and azimuthal angles reconstructed by the rear GEM tracker, while
 1008 the middle panels display the difference between the actual and reconstructed
 1009 angles. The bottom panels show the correlation between the GEM-track angle
 1010 and the angle reconstructed from the hit coordinate in HCAL.

1011 4.4 Determination of G_E^n/G_M^n from Simulated Azimuthal 1012 Asymmetries

1013 The effects of finite size and imperfect reconstruction of the scattering process
 1014 have been investigated using the polarimeter simulation. Multiple scattering in
 1015 the analyzer effectively depolarizes the neutrons as the original reaction plane
 1016 is lost, but the analyzer also requires to be sufficiently thick that a reasonable
 1017 efficiency is maintained. New measurements from Dubna show that high values
 1018 of analyzing power are obtained if the transverse momentum $P_t = P_N^{inc} \sin \theta_N \sim$
 1019 $0.2 - 0.85$ GeV/c so that optimum polar scattering angles fall in the range $2^\circ -$
 1020 15° , dependent on incident momentum. The present geometry of the analyzer
 1021 and GEM trackers produces a polar angle resolution of $\sim 0.05^\circ$ and azimuthal
 1022 resolution of $\sim 0.6^\circ$ which is more than adequate.

1023 Investigations have focused initially on dilution effects in the neutron polarime-
 1024 ter. For this the incident neutrons have been assigned $P_x = 0.19$ $P_y = 0.52$
 1025 which are typical of values expected, and the analyzing power set to 1 in order
 1026 to obtain reasonable Monte Carlo precision. Calculations have been made at
 1027 incident momenta of 1.72 - 5.82 GeV/c, with the HCAL threshold set at 50% of
 1028 the peak channel in the pulse-height distribution.

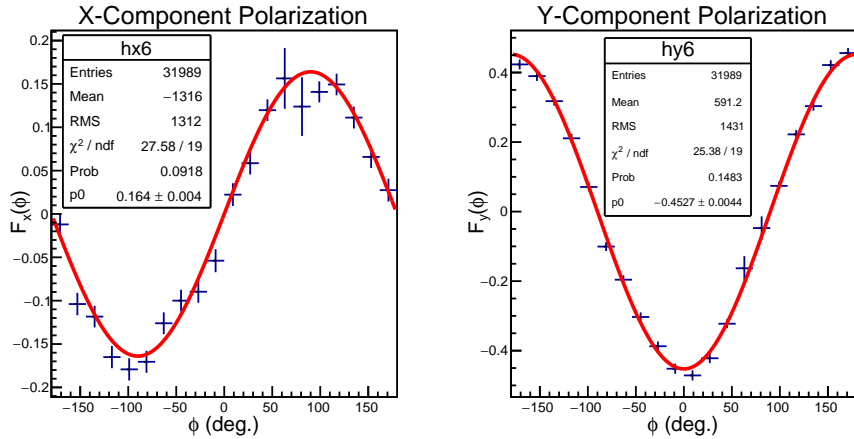


Figure 18: Simulated azimuthal distributions (Eq.15) at an incident neutron momentum of 3.15 GeV/c ($Q^2 = 4.5$ (GeV/c) 2 setting). The red curves are sine and cosine fits to $F_x(\phi)$ and $F_y(\phi)$ respectively.

1029 The polarimeter will measure 4 combinations of the effective neutron polariza-

1030 tions in the x and y directions: $P_x^* = A_y^{eff} P_e P_x$ and $P_y^* = A_y^{eff} P_e P_z \sin \chi$,
 1031 where A_y^{eff} is the effective analyzing power, $P_{x,z}$ are the x and z components
 1032 of the recoil neutron polarization, P_e is the electron beam polarization (0.80)
 1033 and χ is the angle of precession from $z \rightarrow y$ (Table6). With the azimuthal
 1034 distribution described by

$$F(\phi'_n) = C\{1 \pm |P_x^*| \sin \phi'_n \pm |P_y^*| \cos \phi'_n\}$$

1035 then the four possible \pm combinations are labeled F_{++} , F_{--} , F_{+-} , F_{-+} cor-
 1036 respond to the four combinations of beam helicity flip ($P_{x,y}^* \rightarrow -P_{x,y}^*$) and
 1037 the change of polarity of the 48D48 dipole ($P_y^* \rightarrow -P_y^*$). These may be used
 1038 to separate the (relatively small) x component from the y . The unpolarized
 1039 background and x, y components are given by:

$$C = (F_{++} + F_{--} + F_{+-} + F_{-+}) \quad (15)$$

$$F_x = (F_{++} - F_{-+} + F_{+-} - F_{--}) / C$$

$$F_y = (F_{++} - F_{+-} + F_{-+} - F_{--}) / C$$

1042 $F_{x,y}$ are then fitted with sine and cosine functions to obtain the values of $P_{x,y}^*$
 1043 and their uncertainties $\delta P_{x,y}^*$. From this the estimated relative precision $\delta R/R$
 1044 of the ratio $R = G_E/G_M$ may be derived.

$$\frac{\delta R}{R} = \sqrt{\left(\frac{\delta P_x^*}{P_x^*}\right)^2 + \left(\frac{\delta P_y^*}{P_y^*}\right)^2} \quad (16)$$

p_n	A_y^x	A_y^y
1.72	0.91 ± 0.03	0.93 ± 0.01
2.89	0.91 ± 0.03	0.93 ± 0.01
3.15	0.86 ± 0.02	0.86 ± 0.01
3.97	0.92 ± 0.03	0.92 ± 0.01
5.82	0.85 ± 0.03	0.89 ± 0.01

Table 2: Effective polarimeter analyzing powers for x and y components of polarization at different incident neutron momentum p_n

1045 Fig.18 shows simulated azimuthal scattering distributions made with $P_x^* =$
 1046 ± 0.19 , $P_z^* = \pm 0.52$ and $A_y^{eff}(p_n, \theta'_n) = 1.0$ calculated as described above. The
 1047 incident momentum p_n was 3.15 GeV/c, corresponding to the $Q^2 = 4.5$ (GeV/c)²
 1048 kinematic setting, and the total number of incident neutrons simulated was
 1049 4×10^6 . From the sine and cosine fits to F_x and F_y the effective analyzing
 1050 power for the x-component is $A_y^x = 0.86 \pm 0.02$, while for the y-component it is
 1051 $A_y^y = 0.86 \pm 0.01$. Table 2 shows the results for a range of incident neutron mo-
 1052 menta. There seems to be no significant difference between x- and y-component
 1053 analyzing powers, little significant dependence on incident momentum and the
 1054 dilution factor of ~ 0.9 does not vary significantly with incident momentum.

1055 The Dubna polarimeter covered a very similar angular range to the present
 1056 device, used the same 4 cm Cu as an analyzer and employed almost identical

1057 calorimeter modules to select high-energy, forward-angle particles. We therefore
 1058 assume that this polarimeter had a very similar dilution factor to the present
 1059 one. This is already contained within the asymmetries measured at Dubna, and
 1060 thus we have not applied any dilution correction.

1061 Monte Carlo calculations have been performed, with a polarimeter analyz-
 1062 ing power taken from a fit to the p_t dependence of the recent Dubna data.
 1063 This checks that the precision in extracting polarization components, described
 1064 above, is consistent with the simple estimate (Eq.12). Results are displayed in
 1065 Fig.19. Scaling the amplitudes of the fitted asymmetries to the input polar-
 1066 izations (as above) the uncertainties in polarization are $\delta P_x = 0.0292$, $\delta P_y =$
 1067 0.0291 . From Eq.11 and the FoM at 3.15 GeV/c (Fig. 8), $\delta P = 0.0295$ for
 1068 8×10^6 incident neutrons. The actual experiment proposes to collect 18×10^6
 1069 quasi-elastic neutrons at the equivalent setting $Q^2 = 4.5$ (GeV/c) 2 (Table 7).

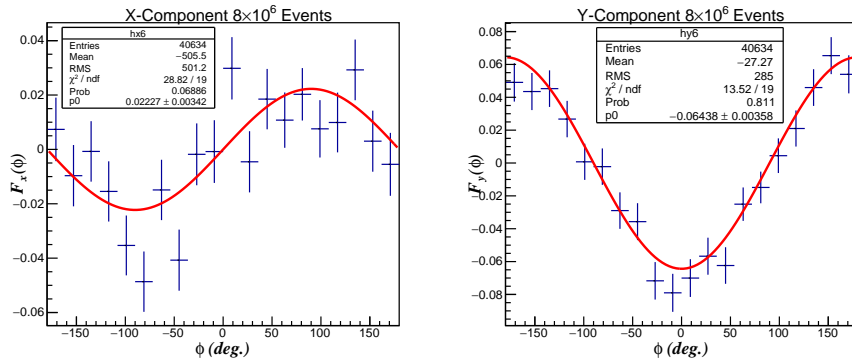


Figure 19: Distributions $F_x(\phi)$ and $F_y(\phi)$ (Eq.15) for $P_x = 0.19$, $P_y = 0.52$ for A_y taken from a fit to the Dubna asymmetry data.

1070 Thus there is reasonable consistency to the procedure and Eq.11,12 provides a
 1071 reasonable approximation when assessing necessary counting time.

1072 4.5 Kinematics

1073 Kinematic settings have been calculated for $Q^2 = 4.5, 6.0, 9.3$ (GeV/c) 2 and
 1074 are summarized in Table 3. The nominal “central” values of the momenta and
 1075 angles relate to free $n(e, e'n)$. Note that the beam-time request of this proposal
 1076 only concerns the $Q^2 = 4.5(\text{GeV/c})^2$ point. Extractions at the larger Q^2 points
 1077 are included to highlight the potential of exploiting the charge-exchange channel
 1078 to reach the highest Q^2 values.

1079 The ranges of kinematic variables for the nominal settings of the large acceptance
 1080 detector system were calculated for quasi-free $^2\text{H}(e, e'n)$, where the internal
 1081 momentum distribution of the neutron was sampled from $p_N^2 \cdot \exp(-p_N^2/2\sigma_N^2)$,
 1082 $\sigma_N = 0.03$ GeV/c, i.e. the Fermi momentum distribution was approximated
 1083 by a Gaussian of width 0.03 GeV/c. Events were generated along the 10 cm
 1084 length of the target and scattered electrons were detected within the effective
 1085 250×750 mm aperture of BigBite situated ~ 2 m from the target center. It
 1086 was also checked if the recoiling neutron is within the acceptance of the 48D48

Setting	Q^2 (GeV/c) ²	E_e (GeV)	$p_{e'}$ (GeV)	θ_e (deg.)	θ_n (deg.)
1	4.5	4.4	2.01	41.9	24.7
2	6.0	6.6	3.40	30.0	25.0
3	9.3	8.8	3.81	30.7	19.4

Table 3: Kinematic Settings. Elastic n(e,e'n) central values. This proposal concerns the $Q^2 = 4.5(\text{GeV}/c)^2$ point only. The higher Q^2 values are included to highlight the potential value of exploiting the charge exchange channel should this technique work as projected.

1087 aperture. At the employed e' scattering angles, BigBite subtends a solid angle
1088 of 58.7 msr and in the worst case 87% of neutrons recoiling after quasi-elastic
1089 ${}^2\text{H}(e, e'n)$ pass through the aperture of the 48D48. The calculated ${}^2\text{H}(e, e'n)$
1090 solid angle is given in Table 7. Fig. 20 A displays the calculated coverage in
1091 Q^2 while the BigBite angular acceptance and corresponding ${}^2\text{H}(e, e'n)$ neutron
1092 acceptance are shown in Fig.20 B - D for kinematic settings 1 - 3 of Table 3.

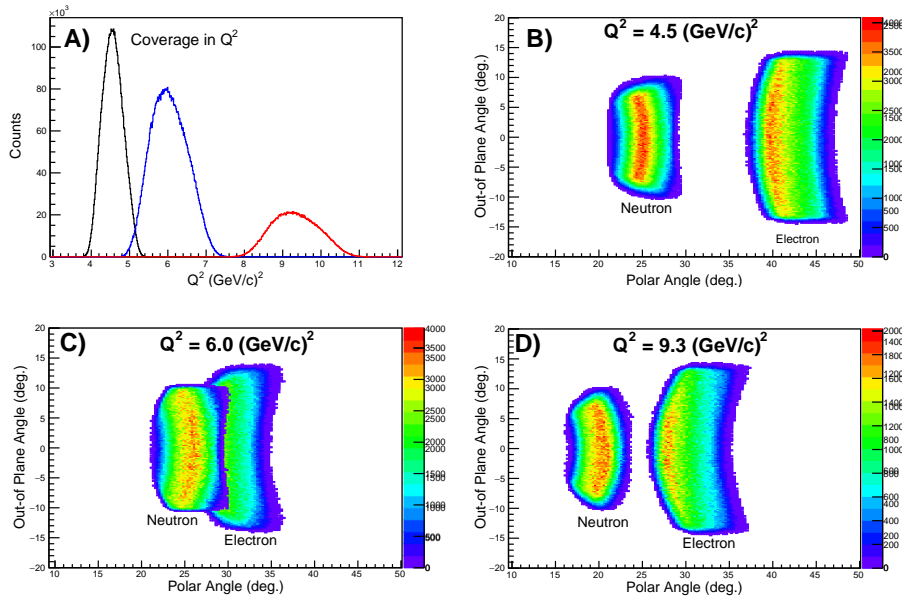


Figure 20: A) range of Q^2 for the nominal settings of Table 3. The distributions are weighted by the Mott cross section. B) electron/neutron angular coverage of BigBite/SBS at $Q^2 = 4.5$ (GeV/c)². [C) Angular coverage at $Q^2 = 6.0$ (GeV/c)². D) Angular coverage at $Q^2 = 9.3$ (GeV/c)²].

1093 4.6 Background Rates and the Trigger Rate

1094 Detector rates have been evaluated using the SBS Monte Carlo simulation which
1095 models the detectors, magnets, the target and its vacuum chamber, beam lines
1096 and the concrete floor of Hall A. Two procedures have been used to generate
1097 events.

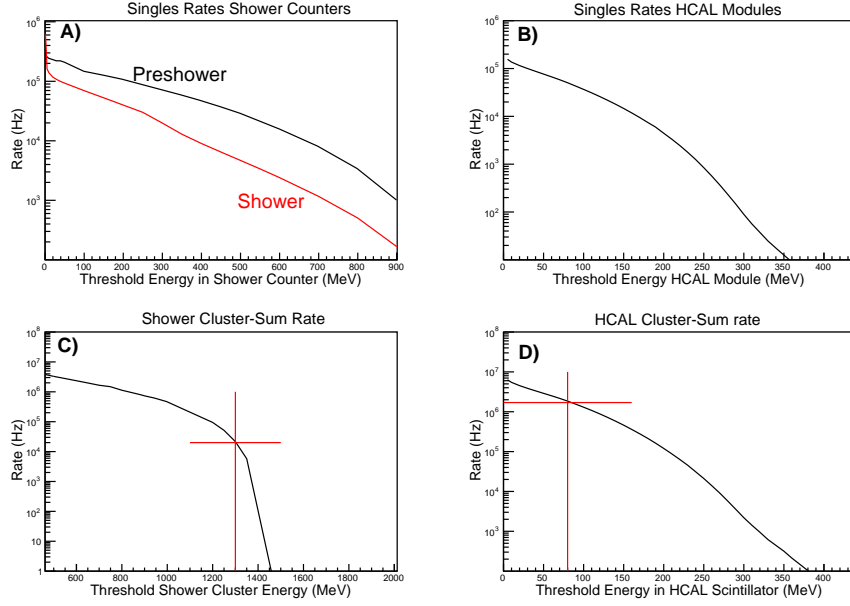


Figure 21: A) Singles rates in the BigBite Pb-Glass preshower and shower counters. B) Singles rates in the hadron calorimeter HCAL modules. C) Cluster-sum rates in the BigBite shower counters. The red cross shows the rate at an applied threshold of 1300 MeV. D) Hadron calorimeter cluster-sum rates. The red cross shows the rate at an applied threshold of 80 MeV. The calculation used procedure 2 (see text).

1. Geant4: electrons of a given beam energy are incident on the 10 cm LD_2 target and Geant-4 samples the interaction mechanism to produce final state particles. Interaction mechanisms included electromagnetic, low-energy electromagnetic, photo- and electro-nuclear, hadronic and high-precision (low-energy) hadronic particle.
2. QFS/EPC + Geant4: Inclusive cross sections, as a function of particle polar angle and momentum, were calculated using the QFS code for $e + {}^2H \rightarrow e' + X$ and EPC code for $e + {}^2H \rightarrow h$, where $h = p, n, \pi^0, \pi^-, \pi^+$. Both codes are described in Ref.[54]. The obtained 2D distributions of angle and momentum were then used to generate events randomly inside the LD_2 target volume, which were then tracked through the detector system by the Geant-4 simulation.

In both cases the output from the Monte Carlo simulation was analyzed to produce numbers of counts in detector elements as a function of applied energy threshold and these numbers were then scaled to an incident neutron luminosity of $1.25 \times 10^{38} s^{-1} cm^{-2}$.

Using procedure 1 a large number of events are necessary in order to generate a reasonable sample of background counts. It is useful to estimate backgrounds from low-energy electromagnetic processes and also low energy neutron processes. Soft electron/positron background from the target region is swept out

Tracking Plane	Rate (kHz/cm ²) 4.5 (GeV/c) ²
GEM-1	26
GEM-2	34
GEM-3	34
GEM-4	7
GEM-5	14
GEM-6	19
CDet-7	2.7 (420)

Table 4: Estimated average rates (kHz/cm²) for tracking planes 1-7 of the polarimeter for the 4.5 (GeV/c)² kinematic setting. The calculation used procedure 1 (see text). GEM-1 is closest to the target. The figures in brackets give the average rate (kHz) in a $51 \times 3 \times 0.5$ cm plastic scintillator element of the CDet. These numbers

Kinematics	Procedure	Shower (kHz)	HCAL (kHz)	Coincidence (kHz)
4.5 (GeV/c) ²	1: G4	14	2200	1.54
4.5 (GeV/c) ²	2: EPC + G4	20	1700	1.70

Table 5: Trigger rates in the Shower and Hadron calorimeters and the Shower-Hadron coincidence rate within a 50 ns window. Procedure is explained in the text.

of detector acceptance by the magnetic fields of the spectrometers, and much of the background registered by the GEM chambers is from soft photons. The exit beamline also produces significant background and detailed studies are currently being made for the G_M^n/G_M^p experiment E12-09-019 to optimize shielding around the beam line.

Procedure 2 is faster and more useful for generating a reasonable sample of higher energy hadronic background, which has a greater bearing on trigger rates in the BigBite electromagnetic calorimeter and the hadron calorimeter HCAL, where cluster-summed energy thresholds are set high. The 48D48 field sweeps charged pions and protons below ~ 1 GeV/c out of the acceptance of HCAL, but significant numbers of higher momentum charged particles, neutrons and photons from π^0 decay do interact.

Fig. 21 A,B displays the estimated singles rates, calculated using procedure 2, in elements of the BigBite electromagnetic calorimeter and the polarimeter hadron calorimeter. Table 4 gives the rates (in kHz/cm²) of the GEM and CDet tracking detectors of the polarimeter calculated using procedure 1. The projected tracker rates, although substantial, are around an order of magnitude lower than expected for the G_E^p/G_M^p experiment. If the QE “spot” at the analyzer for 4.5 (GeV/c)² kinematics has an area of ~ 110 cm² the summed GEM-3 rate within that spot is ~ 3.7 MHz. This translates to a $\sim 25\%$ chance of an accidental hit within a coincidence resolving time of 50 ns.

The shower and hadron calorimeters are equipped with cluster-processing hardware such that a high threshold can be set on the cluster-summed energy to

1141 suppress soft background. Cluster rates as a function of applied threshold are
 1142 displayed in Fig. 21 C,D for the electromagnetic and hadron calorimeters re-
 1143 spectively. The red crosses denote the applied threshold levels, set at $0.65 \times E_{e'}$
 1144 for the Shower calorimeter and $0.5 \times E_{peak}$ (Fig. 11) for the Hadron calorimeter.
 1145 The rates at these applied thresholds are listed in Table 5 and the numbers
 1146 obtained using MC procedures 1 and 2 are reasonably consistent. Projected
 1147 coincidence rates between the electron and hadron-arm calorimeters, within a
 1148 50 ns window, are well within the expected capability of the SBS DAQ system.
 1149 Should a further reduction in the raw trigger rate prove to be desirable, this will
 1150 be possible via the GRINCH gas Cherenkov on the electron arm. According to
 1151 the EPC calculation, around 95% of the shower trigger rate is due to photons
 1152 produced by π^0 decay. Investigation of the inclusion of GRINCH signals into
 1153 the trigger system is in progress.

1154 4.7 Inelastic Background Rejection

1155 With a front GEM tracker in position, it will be possible to separate quasi-
 1156 elastic proton and neutron events cleanly. Inelastic processes, largely associated
 1157 with pion electroproduction, constitute potential sources of background to the
 1158 quasi-elastic ${}^2H(e, e'n)$ signal. Contamination of the electron-arm, quasi-elastic
 1159 (QE) event sample by charged pions is expected to be extremely small due
 1160 to the GRINCH gas Cherenkov in conjunction with PreShower-Shower pulse
 1161 height correlation. The GRINCH will also be very effective at suppressing the
 1162 photons from π^0 production. However the ${}^2H(e, e')$ signal will itself contain
 1163 non-QE background which is estimated in the following, along with a simple
 1164 but effective method of suppression.

1165 It is expected that the present experiment, using a 2H target will have signifi-
 1166 cantly better separation of the QE signal than experiments which employ a 3He
 1167 target. The present experiment is similar in many respects to experiment E12-
 1168 09-019 to measure G_M^n/G_M^p [2], which also employs BigBite on the electron arm
 1169 and the HCAL array on the nucleon arm. The momentum and angle resolutions
 1170 are going to be the same on the electron arm and the angular resolution on the
 1171 hadron arm will be better in the present case.

1172 Modelling of the QE and background channels is based on the code QFS [54].
 1173 This phenomenological model gives a good account of inclusive (e, e') cross sec-
 1174 tions at incident energies of a few GeV and is used to generate the differential
 1175 cross section $\sigma(\omega, \theta_q)$ for ${}^2H(e, e')$. Four reaction mechanisms have been con-
 1176 sidered: quasi-elastic scattering, quasi-deuteron absorption, resonance pion pro-
 1177 duction (resonances at 1232, 1500, 1700 MeV) and deep inelastic scattering. The
 1178 cross sections are then used in an event generator for a Monte Carlo procedure
 1179 to calculate nucleon distributions after $\gamma^* + d \rightarrow n + X$. The angular acceptances
 1180 of BigBite and the neutron polarimeter are included in the calculation. Fig. 22
 1181 shows calculated distributions of W^2 and θ_{qn} , where θ_{qn} is the angle between
 1182 the virtual photon and the final-state neutron. Summed background includes
 1183 pion electroproduction, quasi-deuteron absorption and deep inelastic scattering,
 1184 with pion electroproduction via the $\Delta(1232)$ the dominant contributor. After
 1185 application of a cut on W^2 and θ_{qn} (red box Fig. 22(Right)), 98.6% of the quasi
 1186 elastic events survive and leakage of background events accounts for 1.5% of the
 1187 quasi-elastic strength. The calculation includes the effects of BigBite angle and

momentum resolution and the neutron polarimeter angle resolution, but these are small compared to the intrinsic widths of the QE distributions.

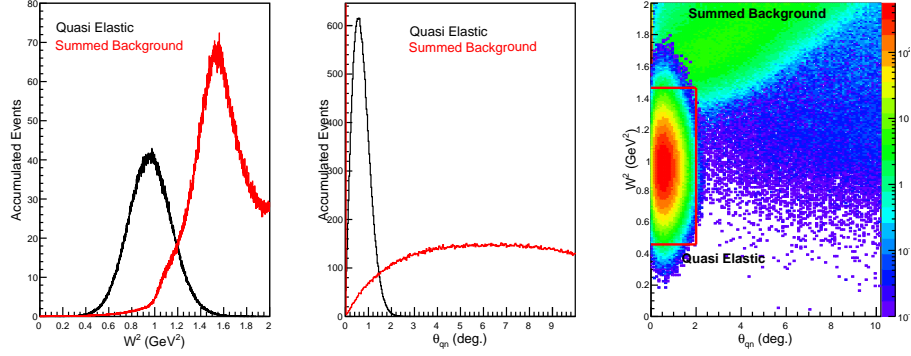


Figure 22: Separation of quasi-elastic and inelastic events for $d(e, e'n)$ events at $Q^2 = 4.5 \text{ (GeV/c)}^2$. Left: separation in terms of W^2 . Middle: separation in terms of θ_{qn} . The QE signal is in black, inelastic background in red. Right: W^2 vs. θ_{qn} distributions. Note that the z-scale is logarithmic. The red box shows the area used to select quasi elastic events.

4.8 Systematic Uncertainties

Potential sources of experimental systematic error are :

- The beam polarization is estimated as 80%, which affects the experimental precision, but the absolute value cancels in a ratio measurement. The electron beam helicity is flipped at a frequency of 30 Hz. The systematic uncertainty is assumed to be negligible.
- The analyzing power uncertainty cancels in a P_x/P_y ratio measurement, assuming it is the same for x and y components of neutron polarization. Polarimeter simulations (Sec. 4.4) do not show any significant variations and we estimate that the maximum size of an error of the ratio is $\sim 1\%$.
- Azimuthal angle acceptance non-uniformity, which should cancel after beam helicity flip and precession angle reversal (reversal of 48D48 field). Monte Carlo calculations are consistent with this and the precision of the calculation limits the size of a potential effect to a maximum of $\sim 1\%$.
- Separation of P_x from P_z does not rely on variation of the magnitude of the spin-precession magnetic field. In the present experiment P_x and P_z ($P_z \rightarrow P_y$) are measured simultaneously with the same precession field, so that potential effects of changes to the background counting rates on the measured asymmetry are thus avoided. Non-uniformity of the magnetic field results in a small amount of $P_z \rightarrow P_x$ mixing. Given that the neutron interaction position at the analyzer can be reconstructed with good accuracy, the neutron path through the dipole can be reconstructed

- 1212 accurately and this this effect corrected with an overall uncertainty of 1%
1213 (Sec. 4.1)
- 1214 • Reproducibility of the spin precession angle after polarity reversal. At a
1215 precession angle of 60° , a 2% difference in integrated field would give 1%
1216 difference in rotated component $P_z \rightarrow P_y$. The 48D48 field strength will
1217 be monitored continuously during an experiment.
 - 1218 • Variation in the angle of spin precession through the dipole magnet. The
1219 path of a neutron through the dipole can be reconstructed with sufficient
1220 precision that a correction factor can be evaluated event by event. The
1221 estimated uncertainty is 0.25%.
 - 1222 • The vertical distribution of counting rates in the polarimeter will change
1223 when the polarity of the spin precession dipole is reversed. Any significant
1224 effect from changes to the level of signal contamination will show up when
1225 different combinations of beam-helicity-flip and dipole-flip asymmetries
1226 are compared.
 - 1227 • Dilution of the asymmetry by accidental background. The background is
1228 estimated to be at the 1% level (Sec.4.6) which can be subtracted without
1229 significant error.
 - 1230 • Contamination of the quasi-elastic signal by inelastic processes. Compared
1231 to ${}^3\text{He}$, a deuteron measurement will have cleaner rejection of the inelastic
1232 background. An estimate of 1.5% is made (Sec. 4.7), based on Monte
1233 Carlo calculations of the amount of contamination of the QE signal by
1234 background processes.
- 1235 Overall we estimate that a 3% systematic error or better is achievable.

1236 5 Estimates of Experimental Precision

1237 The estimate of experimental uncertainty in the ratio $R = G_E^n/G_M^n$ is based on
1238 the following:

- 1239 1. The expected degree of polarization of the incident electrons. Previous
1240 measurements indicate that values in excess of 0.8 are generally available
1241 and we use the value 0.8 for the following estimates.
- 1242 2. The acceptance of BigBite and the polarimeter for quasi elastic ${}^2\text{H}(e, e'n)$.
1243 The kinematic settings are given in Sec.4.5.
- 1244 3. The predicted detection efficiency and acceptance of the polarimeter is
1245 based on Monte Carlo simulations. The overall efficiency of the polarime-
1246 ter, after scattering angle selection, is around 2-3%.
- 1247 4. The analyzing power of $n+\text{Cu} \rightarrow p + X$ has been measured at JINR Dubna
1248 (Sec. 7) at a momentum of 3.75 GeV/c and the procedure to calculate the
1249 FoM for the proposed kinematic settings is described in Sec.2.2.1. The
1250 polarimeter figure of merit F^2 has been obtained from a Monte Carlo eval-
1251 uation of Eq.11, and the uncertainty in polarization from an asymmetry
1252 measurement from Eq.12.

1253 5. The counting rate and polarization uncertainty estimate (Table 7) is based
1254 on a luminosity of $1.25 \times 10^{38} \text{ s}^{-1} \text{ cm}^{-2}$ per nucleon and the cross section
1255 and polarization for free $n(e, e'n)$ scattering. Estimates of elastic cross
1256 section and polarization use the Galster [56] parametrization for G_E^n and
1257 the Kelly parametrization for G_M^n [57]. The dependence of the estimated
1258 precision on the assumed parametrization is very weak.

Q^2 (GeV/c) ²	p_n^{lab} GeV/c	$P_e P_x$	$P_e P_z$	F^2 $\times 10^{-4}$
4.5	3.15	0.082	0.636	2.53
6.0	3.97	0.071	0.555	2.53
9.3	5.82	0.067	0.609	3.08

Table 6: Mean values of projected polarization parameters for the proposed measurement at 4.5 (GeV/c)². Values at the higher Q^2 points are included to highlight the projected potential of this reaction channel in any future high- Q^2 G_E^n experiment.

Q^2 (GeV/c) ²	$\Omega_{e',n}$ (msr)	$\sigma_n(\theta)$ (pb/sr)	Rate (Hz)	Time (hr)	δP $\times 10^{-3}$	δR	
						(stat)	(sys)
4.5	57.4	6.74	48.8	100	19.4	0.078	0.01
6.0	50.8	4.06	26.0	150	23.7	0.12	0.01
9.3	57.6	0.40	2.94	750	28.6	0.17	0.01

Table 7: Counting rate and error estimate for $^2H(\vec{e}, e' \vec{n})$ at an incident (neutron) luminosity of $1.26 \times 10^{38} \text{ cm}^{-2} \text{ s}^{-1}$. “Rate” is the mean $n(e, e'n)$ rate incident on the analyzer, δP is the statistical uncertainty in the polarization, δR (stat) is the statistical uncertainty in the ratio $R = G_E^n/G_M^n$ and δR (sys) is the systematic uncertainty (3% of R). As before, values at the two higher Q^2 points are included to highlight the projected potential of this reaction channel in any future high- Q^2 G_E^n experiment.

1259 Table 6 displays parameters relevant to the precision of the polarization mea-
1260 surement for neutron momenta (p_n^{lab}) associated with the present kinematic
1261 settings (Table 3). Table 7 gives estimates of the counting rate and projected
1262 precisions for the polarization δP and the ratio δR , $R = G_E^n/G_M^n$. The pro-
1263 jected systematic uncertainty is also given, but this is small in comparison to
1264 the statistical uncertainty.

1265 6 Beam Time Request

1266 Beam time is requested (Table 9) to measure G_E^n/G_M^n at one value of Q^2 . Elec-
1267 tron beam helicity flip is performed at 30 Hz, so that combination with the
1268 up-down polarized data along with positive and negative field settings on the
1269 neutron polarimeter dipole will yield the effectively unpolarized azimuthal dis-
1270 tributions in the polarimeter.

1271 At each Q^2 point we will measure at two equal, but opposite polarity setting of
1272 the spin-precession dipole. This will effectively reverse the P_y (precessed from

1273 P_z), to make the separation procedure of x and z (precessed to y) components
 1274 of the recoil-neutron polarization more robust and provide an extra check on
 1275 possible instrumental effects.

1276 In order to determine the four-momentum of the virtual photon to best accuracy,
 1277 the optics of BigBite has to be well known. We propose to use the calibrations
 1278 made for E12-09-019 at an identical kinematic setting. Data will be taken with
 1279 a multi-foil carbon target and a removable sieve slit of lead, located at the front
 1280 face of the magnet. These provide the means to calibrate accurately the angular
 1281 coordinates before magnetic deflection and also the scattering vertex position.
 1282 The momentum calibration is obtained from elastic $e - p$ scattering from a LH_2
 1283 target, where the kinematics are very similar to the quasi-elastic $e - n$ case, so
 1284 that detectors do not require to be moved.

1285 6.0.1 $Q^2 = 4.5 \text{ (GeV/c)}^2$

1286 **The beam time request is for a single kinematic point.** The kinematics
 1287 for the $Q^2 = 4.5 \text{ (GeV/c)}^2$ setting has been chosen to be identical to that
 1288 employed for the G_M^n/G_M^p experiment E12-09-019, which is scheduled to be the
 1289 first SBS experiment to run in Hall A. Apart from the neutron polarimeter,
 1290 the present experiment uses identical apparatus to E12-09-019 so that BigBite
 1291 and HCAL settings could be reused without change. Calibration runs made
 1292 for E12-09-019 could also be reused. The components of the polarimeter will
 1293 be designed to be moved quickly in and out of the acceptance of the hadron
 1294 arm and could be pre-prepared before the start of E12-09-019 for fast insertion
 1295 after a cross section measurement at $Q^2 = 4.5 \text{ (GeV/c)}^2$ has taken place. Thus
 1296 a modest extension of 96 hr production running and 12 hr setup to the E12-
 1297 09-019 beam time would yield a data point for G_E^n/G_M^n which extends the Q^2
 1298 range of world data from 3.4 (GeV/c)^2 to 4.5 (GeV/c)^2 . It would also serve
 1299 as a check that the projections of the experimental uncertainties are accurate,
 1300 before additional beam time is scheduled. A break down of the requested time
 1301 is given in Table 8

Q^2	Function	Target	Precession	Time (hr)
	Insert Polarimeter into E12-09-019 setup			12
4.5	Production $^2H(\vec{e}, e'\vec{n})$	LD_2	pos	48
4.5	Production $^2H(\vec{e}, e'\vec{n})$	LD_2	neg	48
4.5	Use E12-09-019 BB optics calibration	C Foil		0
4.5	Use E12-09-019 momentum calibration	LH_2		0
Total				108

Table 8: Breakdown of Beam Time Request

1302 6.0.2 $Q^2 = 6.0, 9.3 \text{ (GeV/c)}^2$

1303 We include an estimate of the beam time necessary to measure G_E^n/G_M^n by
 1304 charge-exchange neutron scattering at the the kinematic settings $Q^2 = 6.0, 9.3 \text{ (GeV/c)}^2$.
 1305 At this stage **we do not request time** for these points, but propose to re-

turn to the PAC once the performance of this approach has been verified at $Q^2 = 4.5 \text{ (GeV/c)}^2$.

The kinematic points have been chosen to maximize the experimental counting rate and are somewhat different to those proposed for E12-09-019. However whatever the design of the experiment, a dedicated measurement will be necessary to achieve high Q^2 . Due to the rapidly falling cross section, high Q^2 requires more production time to achieve a precision with the power to discriminate between theoretical models. An estimate of the beam-time breakdown of a charge-exchange experiment is given in Table 9. BigBite optics and momentum calibrations would be necessary at each point, as well as time to move the spectrometers to new angles. In total these data points would require 900 hr of production running, 120 hr for calibrations with beam and 12 hr for a configuration change.

Q^2	Function	Target	Precession	Time (hr)
6.0	Production $^2H(\vec{e}, e'\vec{n})$	LD ₂	pos	75
6.0	Production $^2H(\vec{e}, e'\vec{n})$	LD ₂	neg	75
6.0	BB Optics etc.	C Foil		24
6.0	$^1H(e, e'p)$	LH ₂		24
	Angle Change			12
9.3	Production $^2H(\vec{e}, e'\vec{n})$	LD ₂	pos	375
9.3	Production $^2H(\vec{e}, e'\vec{n})$	LD ₂	neg	375
9.3	BB Optics etc.	C Foil		24
9.3	$^1H(e, e'p)$	LH ₂		48
Total				1032

Table 9: Breakdown of beam time estimate for potential future kinematic points

7 Summary and Comparison with other G_E^n/G_M^n measurements at Jefferson Lab.

We propose to measure the ratio G_E^n/G_M^n from a double-polarization asymmetry, using the longitudinally polarized CEBAF electron beam and a polarimeter to measure the transfer of polarization to the recoiling neutron in quasi-elastic $^2H(\vec{e}, e'\vec{n})$. The measurement will be made at one value of the squared four-momentum transfer of the scattered electron: $Q^2 = 4.5 \text{ (GeV/c)}^2$. This data point will not only provide highest Q^2 G_E^n/G_M^n measurement worldwide, but also provide vital data for future experiments at higher Q^2 . With these future data points the unknown behavior of G_E^n/G_M^n at moderate Q^2 will be determined, thus discriminating between the very different behaviors (Fig. 23) predicted by different nucleon-structure models. In particular they will show if the ratio bends over and heads towards zero with increasing Q^2 , as predicted by recent DSE calculations or continues to increase with increasing Q^2 . Since the availability of G_E^n data determines the Q^2 range over which $u - d$ flavor separation of $F_1(Q^2)$ and $F_2(Q^2)$ is possible, the present and future data would also result in a large extension in range. With present data, separation is only possible up to 3.4 (GeV/c)^2 .

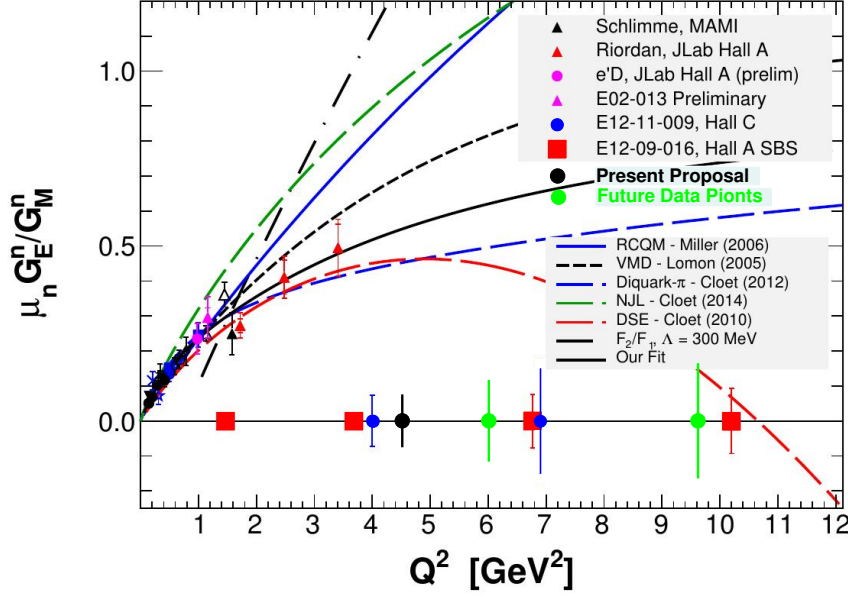


Figure 23: A comparison of the uncertainties of this proposal (black circle) with those of E12-09-016 [1] (red squares) and E12-11-009 (blue circles). The green data points reflect projected uncertainties for a future extended run with the SBS apparatus (Sec. 6.0.2). The blue data points reflect the E12-11-009 (C-GEN) proposal projections that did not include sensitivity to the charge-exchange channel under study here. Data from the proposed measurement will be used to study extensions to the C-GEN polarimeter to enhance its sensitivity to this reaction channel.

1337 The employed apparatus will mainly use components already under construction
1338 for other SBS EMFF experiments and will closely resemble that of E12-09-019
1339 to measure G_M^n/G_M^p . In particular it will employ the same target, electron arm
1340 and calorimeter on the hadron arm. On the hadron arm, a neutron polarimeter
1341 will be constructed by introducing GEM tracking components from E12-07-
1342 109 to measure G_E^p/G_M^p , a Cu block of analyzing material and components to
1343 provide sensitivity to large-angle protons. Thus the polarimeter will measure
1344 asymmetries produced by $\vec{n} + Cu \rightarrow p + X$, $\vec{n} + X \rightarrow p + X$, as well as $\vec{p} + Cu \rightarrow$
1345 $p + X$ from quasi-elastic ${}^2\text{H}(\vec{e}, e' \vec{p})$. This novel approach has been inspired
1346 by new analyzing power data from JINR Dubna on polarized, charge-exchange
1347 scattering at $p_N \sim 4$ GeV/c. Preliminary analyses of these data show sizable
1348 values of the analyzing power..

1349 This experiment will provide critical data to validate the charge-exchange chan-
1350 nel as an effective method for recoil polarimetry. It will probe the sensitivity
1351 and identify challenges associated with this technique, allowing the determina-
1352 tion of an optimal approach to executing a long run at high Q^2 in the future.
1353 Options to be considered include pursuing the measurement within the SBS
1354 configuration in Hall A, through to an enhanced version of the C-GEN design
1355 in Hall C, or a combined approach staged in either Hall.

1356 The Collaboration

1357 This experiment will be performed in Hall-A of Jefferson Laboratory. It will be
1358 part of the SBS program of experiments and the bulk of the necessary major
1359 apparatus (BigBite, the SBS dipole, HCAL, the GEM tracking systems and the
1360 Coordinate Detector) will be used in other experiments. The joint international
1361 effort encompasses groups from the USA (JLab, UVa, CMU, W&M, CNU, HU,
1362 NSU, ISU, NCA&T, JMU, CSU), the UK (UGla), Italy (INFN Catania and
1363 Rome), The Russian Federation (JINR) and Canada (SMU).

1364 We list the institutes which have been involved in building the apparatus re-
1365 quired by the present experiment .

1366 • Jefferson Laboratory (JLab):

1367 JLab supervise the entire SBS programme of experiments. They are re-
1368 sponsible for the design of mechanical structures to hold the apparatus, the
1369 modification of the 48D48 magnet and beam-line vacuum pipe. They will
1370 supervise the installation and commissioning of the upgraded infrastruc-
1371 ture required for the magnet, the targets, the beam line and the BigBite
1372 electron spectrometer. JLab coordinates the design and commissioning of
1373 the diverse pieces of apparatus for SBS experiments and their leadership
1374 is critical in all aspects of the SBS program.

1375 • University of Glasgow (UGla):

1376 UGla have initiated R&D on the polarimeter, have a Ph.D. student work-
1377 ing on this investigation and have participated in the polarized neutron
1378 measurements at JINR Dubna. They are responsible for the new BigBite
1379 timing hodoscope and the “NINO” front-end amplifier/discriminator elec-
1380 tronics used in the GRINCH, Hodoscope, CDet and HCAL, comprising
1381 several thousand channels.

1382 • JINR Dubna (JINR):

1383 JINR lead the effort to measure the analyzing power of polarized neutron
1384 and proton scattering from various materials (CH_2 , CH, C, Cu) at neu-
1385 tron momenta of several GeV/c. This uses the polarized nucleon beams,
1386 derived from polarized deuterons produced by the Nuklotron accelerator
1387 in JINR. They have ensured the necessary provision of beam, apparatus
1388 and subsistence for foreign researchers to carry out the measurement.

1389 • INFN Catania (CATANIA):

1390 CATANIA have made major contributions to HCAL, and electronics for
1391 HCAL and CDet

1392 • INFN Rome (ROME):

1393 ROME lead the effort to build the high-resolution, front tracker GEM
1394 chambers, used in BigBite, and also the design and implementation of the
1395 GEM readout electronics based on the APV25 chip. These detectors also
1396 form the forward trackers of the SBS proton polarimeter and will benefit
1397 all experiments which use the common apparatus.

1398 • University of Virginia (UVa):

1399 UVA group lead the effort to build the large rear GEM chambers, used

1400 in the polarimeter and BigBite, and are also heavily engaged in chamber
 1401 R&D work. These detectors also form the rear trackers of the SBS proton
 1402 polarimeter, as well as the extended tracking system to detect large-angle
 1403 recoiling protons, and will benefit all experiments which use the common
 1404 apparatus. Already UVa have produced more than 40 working 50×60 cm
 1405 GEM modules with electronics, with 8 spares envisaged, sufficient to cover
 1406 the present experiment.

- 1407 • **Carnegie Mellon University (CMU):**
 1408 CMU group lead the construction effort on the hadron calorimeter mod-
 1409 ules. They have optimized the pulse height response and time resolution.
 1410 HCAL will be the high efficiency nucleon detector for several SBS experi-
 1411 ments and will benefit all experiments which use the common apparatus.
- 1412 • **College of William and Mary (W&M):**
 1413 W&M are responsible for the GRINCH gas Cherenkov detector for Big-
 1414 Bite, which will provide more selective triggering on electrons, as well as
 1415 improved $e^- - \pi^-$ separation. This work will benefit all experiments which
 1416 use BigBite.
- 1417 • **Christopher Newport University (CNU):**
 1418 CNU have taken over responsibility for the assembly and testing of mod-
 1419 ules for the Coordinate Detector, which will sit before the hadron calorime-
 1420 ter and provide charged particle identification and vetoing capability. This
 1421 detector is being designed initially for the electron arm of the GEp(5) ex-
 1422 periment, but it is also suitable for use with HCAL and will benefit all
 1423 experiments which use the common apparatus.
- 1424 • **Hampton University (HU)**
 1425 HU have experience with GEM detectors and APV+MPD readout elec-
 1426 tronics from their involvements in OLYMPUS, MUSE and DarkLight. HU
 1427 is located in close proximity to JLab; the group will join the testing, com-
 1428 missioning and installation effort of the GEM modules on-site at Jefferson
 1429 Lab.
- 1430 • **Idaho State University (ISU)**
 1431 ISU have made a large contribution to the initial development of the co-
 1432 ordinate detector.
- 1433 • **North Carolina A&T (NCA&T)**
 1434 NCA&T are actively engaged in the testing and construction of various
 1435 components of the SBS system
- 1436 • **St. Mary's University (SMU):**
 1437 SMU have provided significant contribution to development of the coor-
 1438 dinate detector, notably testing multianode PMTs.
- 1439 • **James Madison University (JMU)**
 1440 JMU have provided effort for testing of photomultipliers used in the GRINCH
 1441 gas Cherenkov and other detectors used for SBS experiments.
- 1442 • **California State University (CSU):**
 1443 CSU have manufactured PMT housings for the BigBite timing hodoscope,
 1444 which exclude He from the PMT.

1445 Cost Estimate of New Components

1446 The BigBite spectrometer, including GEM, GRINCH, EM Calorimeter and
 1447 Timing Hodoscope, and the SBS polarimeter, including 48D48 dipole, GEM,
 1448 Coordinate Detector and HCAL, which are used in this experiment will be built
 1449 for previously approved SBS experiments in Hall A. There will be no additional
 1450 cost for the construction of these elements.

1451 New components or modifications for the polarimeter include:

- 1452 1. A Cu analyzer block is estimated to cost \$5000-10000
- 1453 2. Mechanical modification to the polarimeter mounting platforms is esti-
 1454 mated to be in the region \$20000.
- 1455 3. Additional plastic scintillator bars, including photomultipliers and front-
 1456 end electronics will be configured from existing components available within
 1457 the collaboration.

1458 Appendix A. Measurement of Neutron and Proton 1459 Analyzing Power at JINR Dubna

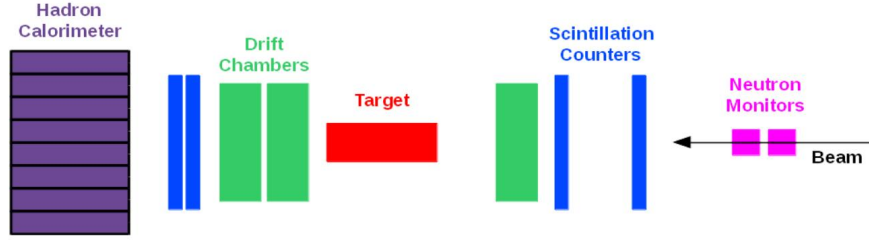


Figure 24: Representative schematic (not to scale) of the Dubna polarimeter. The target is the analyzer material under investigation.

1460 The Dubna experiment [51] measures analyzing powers for different materials
 1461 using polarized neutrons with momentum (p_n) up to 4.5 GeV/c and polarized
 1462 protons with momentum (p_p) up to 7.5 GeV/c [58]. This provides entirely new
 1463 neutron information for $n + Target \rightarrow p + X$ and extends previous proton results
 1464 for $p + CH_2 \rightarrow p + X$ at $p_p = 1.75 - 5.3$ GeV/c [59]. These data are vital for SBS
 1465 measurements of G_E^n/G_M^n and G_E^p/G_M^p . The data were collected in November
 1466 2016 and February 2017.

1467 Neutrons or protons were derived from the breakup of polarized deuterons strik-
 1468 ing a Be target, separated by means of a dipole magnet and then collimated. An
 1469 ionization chamber was used to estimate proton intensities and a polarimeter,
 1470 comprising several scintillation counters located around the proton target, was
 1471 used to give a measurement of the deuteron beam polarization. For neutrons,
 1472 a monitoring system consisting of CH_2 elements and scintillation counters was
 1473 installed after the collimator.

1474 The nucleon polarimeter (Fig. 24) consisted of scintillation counters for trigger-
 1475 ing, a series of drift chambers for charged particle tracking and a segmented
 1476 hadron calorimeter for the detection of final state particles. Several different
 1477 analyzing materials were used, including: 30 cm CH_2 ; 20 cm C; 4 cm Cu, and
 1478 active CH scintillator.

1479 Online analysis of neutron data taken in Feb. 2017 indicated that a Cu target
 1480 has a similar analyzing power to C and produced a factor ~ 3 increase in
 1481 the detected yield of protons. Inclusion of hadron calorimeter cuts, to remove
 1482 events with large scattering angle and low pulse height, increased the obtained
 1483 asymmetries. Pending confirmation of the preliminary analyses, we are not at
 1484 liberty to release any analyzing power information, but this has been used in
 1485 constructing the polarimeter FoM (Sec. 2.2.3) for the present proposal.

1486 References

- 1487 [1] *Measurement of the Neutron Electromagnetic Form Factor Ratio*
 1488 G_E^n/G_M^n at High Q^2 , JLab Experiment E12-09-016, Spokesper-
 1489 sons: G. Cates, S. Riordan, B. Wojtsekhowski. *The Electric*
 1490 *Form Factor of the Neutron with SBS*, S. Riordan, SBS Review,
 1491 March 28, 2012.
- 1492 [2] *Precision Measurement of the Neutron Magnetic Form Factor*
 1493 *at to $Q^2 = 18$ (GeV/c) 2* . Jefferson Lab experiment E12-09-019,
 1494 Spokespersons: J. Annand, R. Gilman, B. Quinn, B. Wojt-
 1495 sekhowski,
- 1496 [3] *Large Acceptance Proton Form Factor Ratio Measurements at 13*
 1497 *and 15 (GeV/c) 2 Using Recoil Polarization Method*, JLab Exper-
 1498 iment E12-07-109, Spokespersons: E. Cisbani, M. Khandaker,
 1499 C.F. Perdrisat, L.P. Pentchev, V. Punjabi, B. Wojtsekhowski.
- 1500 [4] *Precision Measurement of the Proton Elastic Cross Section at*
 1501 *High Q^2* , JLab. experiment E12-07-108, Spokespersons: J. Ar-
 1502 rington, S. Gilad, B. Moffit, B. Wojtsekhowski.
- 1503 [5] *The Neutron Electric Form Factor at Q^2 up to 7 (GeV/c) 2 from*
 1504 *the reaction $^2H(\vec{e}, e'\vec{n})$ via Recoil Polarimetry*. JLab. Experi-
 1505 ment E12-11-009, Spokespersons: B.D. Anderson, J. Arrington,
 1506 S. Kowalski, R. Madey, B. Plaster, A. Yu. Semenov. *E12-11-009*
 1507 *(G_{En}) Update*, M. Kohl, Hall C Users Meeting, Feb. 21-22, 2014.
- 1508 [6] S. Riordan *et al.*, Jefferson Lab experiment E02-013, Phys. Rev.
 1509 Lett. 105(2010), 262302.
- 1510 [7] B. Plaster *et al.*, Phys. Rev. C73(2006), 025205., R. Madey *et*
 1511 *al.*, Phys. Rev. Lett. 91(2003),122002.
- 1512 [8] S.J. Brodsky, G.R. Farrar, Phys. Rev. D11(1975), 1309.
- 1513 [9] M.K. Jones *et al.* Phys. Rev. Lett. 84(2000), 1398.
- 1514 [10] O. Gayou *et al.*, Phys. Rev. Lett. 88(2002), 092301.

1515 [11] V. Punjabi *et al.*, Phys. Rev. C71(2005), 055202.

1516 [12] A.J.R. Puckett *et al.*, Phys. Rev. Lett. 104(2010), 242301.

1517 [13] A. Puckett *et al.*, Phys. Rev. C85(2012),045203.

1518 [14] L. Andivahis *et al.*, Phys. Rev. D50(1994), 5491.

1519 [15] M.E. Christy *et al.*, Phys. Rev. C70(2004), 015206.

1520 [16] I.A. Qatten *et al.*, Phys.Rev.Lett. 94(2005), 142301.

1521 [17] G.D. Cates, C.W. De Jager, S. Riordan and B. Wojtsekhowski,
1522 Phys. Rev. Lett. 106(2011), 252003.

1523 [18] J. Koponen *et al.*, arXiv:1701.04250v1, 16 Jan. 2017

1524 [19] C.D. Roberts and A. G. Williams, Prog. Part. Nucl. Phys.
1525 33(1994), 477.

1526 [20] I.C. Cloët *et al.*, Few-Body Syst., 46 (2009), 1.

1527 [21] J. Segovia *et al.*, Few-Body Syst. 55 (2014), 1185.

1528 [22] D.J. Wilson *et al.*, Phys. Rev. C85(2012),025205.

1529 [23] I.Cloet *et al.*, Phys. Rev. C 90, (2014), 045202.

1530 [24] R. S. Sufian *et al.*, Phys. Rev. D95(2017),014011.

1531 [25] I. A. Qattan and J. Arrington, Phys. Rev. C86(2012),065210.

1532 [26] M.Diehl and P.Kroll, Eur. J. Phys. C73 (2013), 2397.

1533 [27] I. Passchier *et al.*, Phys. Rev. Lett. 82(1999), 4988.

1534 [28] H. Zhu. Phys. Rev. Lett. 87(2001), 081801.

1535 [29] G. Warren *et al.*, Phys. Rev. Lett. 92(2004), 042301.

1536 [30] M. Meyerhoff *et al.* , Phys. Lett. B 327(1994) , 201.

1537 [31] J.Becker *et al.*, Eur. J. Phys. A6(1999), 329.

1538 [32] D.Rohe *et al.*, Phys. Rev. Lett. 83(1999), 4257.

1539 [33] B.S. Schlimme *et al.*, Phys. Rev. Lett. 111(2013), 132504.

1540 [34] T. Eden *et al.*, Phys. Rev. C50(1994), 1749.

1541 [35] C. Herberg *et al.*, Eur. J. Phys. A5(1999), 131.

1542 [36] M. Ostrick *et al.*, Phys. Rev. Lett. 83(1999), 276.

1543 [37] D.I. Glazier *et al.*, Eur. J. Phys. A24(2005), 101.

1544 [38] *Measurement of the Neutron Magnetic Form Factor at High Q²*
1545 *Using the Ratio Method on Deuterium* , JLab. Experiment E12-
1546 07-104, Spokespersons: G.P. Gilfoyle, W.K. Brooks, M.F. Vine-
1547 yard, J.D. Lachniet, L.B. Weinstein, K. Hafidi.

- 1548 [39] A.I. Akhiezer *et al.*, JEPT 33(1957), 765.
- 1549 [40] R.G. Arnold *et al.*, Phys. Rev. C23(1981), 36.
- 1550 [41] M. M. Sargsian *et al.*, Phys. Rev. C 71(2005), 044614.
- 1551 [42] N.V. Vlasov *et al.*, Instr. and Exp. Tech. 49(2006), 49.
- 1552 [43] R. Diebold *et al.*, Phys. Rev. Lett. 35(1975), 632.
- 1553 [44] S.L. Kramer *et al.*, Phys. Rev. D17(1978), 1709.
- 1554 [45] H. Spinka *et al.*, Nucl. Instr. and Meth. A211(1983), 239.
- 1555 [46] L.S. Azhgirey *et al.*, Nucl. Instr. and Meth. A538(2005), 431.
- 1556 [47] N.E. Cheung *et al.*, Nucl. Instr. and Meth. A363(1995), 561.
- 1557 [48] I.G. Alekseev *et al.*, Nucl. Instr. and Meth. A434(1999), 254.
- 1558 [49] P.R. Robrish *et al.*, Phys. Lett. B31 (1970), 617.
- 1559 [50] M.A. Abolins *et al.*, Phys. Rev. Lett. 30 (1973), 1183.
- 1560 [51] *Measurement of analyzing powers for the reaction $p + CH_2$*
1561 *up to 7.5 GeV/c and $n + CH$ up to 4.5 GeV/c at the Nu-*
1562 *clotron*, ALPOM2 proposal to JINR Dubna PAC, March 2015,
1563 Spokespersons: N.M. Piskunov, C.F. Pedrisat, V. Punjabi, E.
1564 Tomasi-Gustafsson.
- 1565 [52] *Analyzing Power of pp and np Elastic Scattering at Momenta*
1566 *between 2000 and 6000 GeV/c and Polarimetry at LHE*, V.P.
1567 Ladygin, JINR report E13-99-123, 1999.
- 1568 [53] TOSCA/Opera-3D, Vector Fields Software, Cobham Technical
1569 Services, Dorset, UK
- 1570 [54] J. W. Lightbody and J. S. O'Connell, Computers in Physics
1571 2(1988),57; <http://dx.doi.org/10.1063/1.168298>
- 1572 [55] P.V. Degtyarenko, computer code DINREG, *Applications of the*
1573 *Photonuclear Fragmentation Model to Radiation Protection Problems*,
1574 Proc. Second Specialist Meeting on Shielding Aspects of Accel-
1575 erators (SATIF2), CERN, October 1995.
- 1576 [56] S. Galster *et al.*, Nucl. Phys. B32 (1971), 221.
- 1577 [57] J. J. Kelly, Phys. Rev. C70(2004), 068202.
- 1578 [58] N.M. Piskunov *et al.*, Physics of Particles and Nuclei, 2014, Vol.
1579 45, No. 1, pp. 330–332.
- 1580 [59] I.M. Sitnik *et al.*, Nuclear Instruments and Methods in Physics
1581 Research A 538 (2005) 431– 441.